

Received February 10, 2020, accepted February 21, 2020, date of publication February 27, 2020, date of current version March 6, 2020.

Digital Object Identifier 10.1109/ACCESS.2020.2976815

Fractal Analysis and Texture Classification of High-Frequency Multiplicative Noise in SAR Sea-Ice Images Based on a Transform-Domain Image Decomposition Method

IMAN HEIDARPOUR SHAHREZAEI¹ AND HYUN-CHEOL KIM¹, (Member, IEEE)

Unit of Arctic Sea-Ice Prediction, Korea Polar Research Institute (KOPRI), Incheon 21990, South Korea

Corresponding author: Hyun-Cheol Kim (kimhc@kopri.re.kr)

This work was supported by the Korea Polar Research Institute (KOPRI) under Grant PE20080 (study on remote sensing for quantitative analysis of changes in the arctic cryosphere).

ABSTRACT Texture in synthetic aperture radar (SAR) images is a combination of the intrinsic texture of scene backscattering and the texture due to noncoherent high-frequency multiplicative noise (HMN) interactions that reflect erroneous information and lead to observation misinterpretation. The focus of this paper is the fractal analysis of KOMPSAT-5 SAR images of noncoherent sea-ice textures while being decomposed by discrete wavelet transform (DWT) processing. As a novel approach, fractal analysis relies on SAR sea-ice spatial backscattering data generation and time-frequency domain (TFD) formulations from the perspective of uncorrelated HMN. To the best of our knowledge, this is the first time that the extraction of the resolution profile and raw data for the reference KOMPSAT-5 SAR sea-ice image have been derived, evaluated and compared both qualitatively and quantitatively at each scale of DWT decomposition on the basis of the presence of HMN. This paper also presents a novel detailed modeling of the multiresolution probability distribution function of the HMN and its power spectral density function modeling at each scale of the decomposition. Other quality assessment techniques, such as two K-means clustering algorithms and several visualized verification methods, such as gradient vector field, advection mapping and tensor field mapping, have been implemented in this regard to investigate embedded HMN suppression and its adverse effects on the presence of pixel anomalies. As a result, as the decomposition continues, the HMN at each scale of decomposition is constantly altering from high-frequency uncorrelated anomalies to low-frequency joint spatial information within the observed 2-D data. In other words, excessive multiscale HMN suppression will result in spatial information loss that makes the DWT scale selection quite important for texture classification. The results also show that the importance of HMN suppression in SAR sea-ice images in the form of pixel anomaly decomposition for the purpose of further texture investigation should be in accordance with the spectral behavior of the HMN. The results are helpful for SAR remote sensing image restoration and data preservation when dealing with high-resolution SAR images, such as in time series analysis, sea-ice texture change detection, and polar structural mapping. The proposed approach is implemented on real KOMPSAT-5 SAR satellite sea-ice images, while fractal spatial resolution profile simulations are carried out based on the inversed equalized hybrid domain image formation algorithm.

INDEX TERMS Discrete wavelet transform, fractal analysis, high-frequency multiplicative noise, raw data generation, synthetic aperture radar.

I. INTRODUCTION

Synthetic aperture radar (SAR), by transmitting wideband signals at specific intervals, can exploit the properties of the backscattered signals pertaining to illuminated terrain under

all-weather and all-day conditions [1]. These backscattered data are unprocessed time-synchronized signals in a complex demodulated format, which are just frame formatted and rearranged into contiguous radar range lines known as raw data [2]. The SAR image formation algorithm (IFA) processes the raw data in both fast and slow times to reconstruct 2-D grayscale images of the illuminated terrain and its

The associate editor coordinating the review of this manuscript and approving it for publication was Junjie Wu.

pertinent textures [2], [3]. During the coherent processing of the successive received pulses, constructive and deconstructive phase interferences occur in the form of pixel anomalies within the image reconstruction procedure known as high-frequency multiplicative noise (HMN) [4]. These signal-dependent anomalies, which present as uncorrelated signals in the form of pixel intensity alterations, will result in image quality degradation and texture misinterpretations [4].

Despite the adverse effects of HMN presence in SAR imagery, they are still the main information source for remote sensing, specifically polar region with hostile conditions and difficult access. Polar region with underlying oceans and overlying atmosphere have directly a role in global climate change studies [2], [5]. Hence, SAR polar observation and sea-ice imagery are particularly helpful for frigid zone monitoring and texture analysis for the purpose of environmental research, climate change studies, earth temperature observation, maritime safe navigation, polar explorations, and other probable operations in ice-covered areas [6]–[8]. In this regard, 2-D grayscale images of SAR sea-ice are processed for the purpose of sea-ice electromagnetic interactions, structure recognition, texture clustering, image classification and image change detection [9], [10].

However, the complex SAR sea-ice terrain is considered a nondeterministic texture completely time-dependent and constantly changing based on origination, formation, growth and melting. In other words, sea-ice has different features, such as surface roughness, temperature, inclusion particles, and salinity, which form different electric permittivity and magnetic permeability values. These values can easily affect the reception procedure of the reflected pulses in the shape of diverse scatterings and various backscattering coefficients by means of uncorrelated HMN, which results in incoherent raw data reception and image pixel anomalies as major sources of information loss and imprecise SAR classifications and detections [4], [7], [11]–[13]. In short, sea-ice textures have different electromagnetic interaction behaviors and gray levels, which might reflect erroneous information and lead to misinterpretations of the observation data, which are very important for polar region observations. Therefore, identifying the main features of sea-ice terrains into a set of predefined categories and objective SAR sea-ice classifications are optimum solutions to avoid texture misinterpretations while handling the presence of HMN.

To date, different approaches have been proposed for SAR sea-ice texture analysis and classification, which are mostly based on the statistical analysis of pixels or generative stochastic parameter modeling [6], [14]–[25]. The computational complexity as well as focusing on the intensity coupling between pixels at a single scale without considering the adverse effects of HMN and the origin of signal anomalies are the major defects of such texture analysis methods proposed in different studies [26].

With the advent of studies on scaling properties, the use of the texture transform method based on time-frequency domain (TFD) techniques has become popular for the

purpose of texture analysis [27]–[32]. Moreover, discrete wavelet transform (DWT) applications for SAR image processing have received much attention in the literature in contrast to other TFD techniques [33]–[36]. With the help of the DWT algorithm, SAR images can not only be transformed into both spatial and frequency domain information as a multiresolution technique but can also be decomposed into further scales, which is referred to as multiscale implementation. Accordingly, a TFD fractal formulation of the SAR sea-ice texture in the presence of embedded HMN and pixel anomalies based on DWT application can be considered a novel SAR sea-ice fractal research study that has not yet been performed on sea-ice textures [4], [7], [9]–[13], [18]–[23], [25]–[36]. In other words, multiresolution DWT decomposition is not only helpful to investigate the adverse effects of the presence of HMN and its suppression within the SAR sea-ice texture but also assists the multiscale probability distribution formulation of noncoherent structures and classification along with preservation of the fine details of the sea-ice. The Korea Multi-Purpose Satellite-5 (KOMPSAT-5) is South Korea's first satellite equipped with X-band SAR. The enhanced observation mode of KOMPSAT-5 can be considered as suitable option for constant monitoring of sea-ice areas, which has not been investigated completely [37]. According to the DWT algorithm, a multiresolution TFD formulation and modeling of the electromagnetic interaction and HMN multiscale probability distribution function (PDF) within the KOMPSAT-5 SAR sea-ice image is a novel key point for such fractal analysis. All the aforementioned works have not only failed to develop a TFD formulation and model the probability distribution of the embedded HMN and pixel anomalies of SAR sea-ice texture but also lack multiscale suppression fractal analysis and the successive classification procedure as well as proper signal-based and objective image quality assessment.

To the best of our knowledge, this is the first time that the adverse effects of the presence of HMN and the associated pixel anomalies within KOMPSAT-5 SAR sea-ice images have been investigated with the help of joint complex TFD formulation and modeling on the basis of multiscale DWT decomposition. The main objectives of this study are the precise multiresolution HMN investigation within the SAR texture and its pertinent effects on the sea-ice classifications while being suppressed by the DWT. This study also includes an objective SAR sea-ice image quality assessment, which verifies the proposed TFD formulation, structural behavioral modeling, signal fractal analysis and classification method. The investigation of the presence of HMN is performed with the help of sea-ice electromagnetic interaction analysis and resolution profile extraction for both the image and the sensor [38]. Additionally, a multiscale TFD distribution formulation of embedded HMN and a model of its spectral behavior as well as different K-means clustering algorithms are also being used for the purpose of fractal sea-ice signal and pixel anomaly investigation. The objective quality metrics include the PDF of HMN, HMN power spectral density (PSD)

modeling, gradient vector mapping, tensor field mapping and advection mapping of the HMN, pixel-based measurements, correlation-based metrics, local entropy and local range measurements as well as SAR-specific parameters such as the peak side-lobe ratio (PSLR) and the integrated side-lobe ratio (ISLR). The K-means classification application is considered as two different iterative and adaptive versions for the purpose of research reliability. All the abovementioned procedures (image resolution investigation, signal spatial profile extraction, multiscale HMN distribution assessment and modeling, image decomposition, K-means classifications and the different objective quality assessment techniques) are considered for the first time as a whole fractal research analysis in the case of real SAR sea-ice texture interpretation, specifically the KOMPSAT-5 SAR. The results verify the formulation, modeling, suppression, decomposition and classification accuracy.

This paper is organized as follows. In Section II, a brief description of SAR electromagnetic interaction and HMN generation is presented. This section also includes KOMPSAT-5 SAR sea-ice resolution profile extraction based on the image profile and raw data generation (RDG) in the presence of HMN. This section also describes DWT decomposition of images, HMN probability distribution formulation and TFD spectral behavior analysis as well as K-means classification. In Section III, the proposed aforementioned methods and the simulations and verification scenarios with the help of the above objective qualitative and quantitative metrics will be applied. Finally, the conclusions are given in Section IV.

II. CONCEPTS AND APPROACHES

A. KOMPSAT-5 SAR SEA-ICE IMAGE ANALYSIS AND RESOLUTIONAL PROFILE EXTRACTION

SAR sensors provide information about terrains by measuring and mapping the reflected energy in microwave bands. In comparison to its passive, optical or infrared counterparts, SAR circumvents the resolution limitation by using coherency in the ranging and Doppler tracking to acquire high-resolution images of terrain based on pulse compression and the effective viewing geometry. Each image pixel is generated by processing a large number of successive echoes and the coherency of the pulse in the transeiving modulation process, which results in a deterministic phase variation is very important. It is important to note that the sensor directly observes the scene reflectivity as a spatially varying quantity, and any random process in the form of dephased reflectance will lead to distinct intensity anomalies in the signal and, consequently, the image texture. In other words, nonstationary multiplicative noise with random interference, known as HMN, degrades the backscattered signal quality and makes the pulse no longer coherent for the reception of the signal. According to the spatial configuration of the noise, the signal characteristics will change, and the spatial distribution of the noise power makes the description of the

raw data matrix highly complex because of changing values. This noncoherent noise is distributed throughout the image and contributes very little to the pixel intensities but can constitute a significant attenuation of the received backscattered raw data profile as the presence of uncorrelated multiplicative interference, which varies randomly. The spatial distribution of the proposed nonstationary multiplicative noise in the time-dependent formulation of the backscattered signal intensity can be presented as the complex reflectivity:

$$\sigma(x, y, t) = \sigma^0(x, y) \cdot N(t) \quad (1)$$

where σ is a product of a spatially varying complex reflectivity $\sigma^0(\cdot)$ and time-dependent HMN in terms of $N(t)$. The HMN is considered completely signal dependent and is demodulated in a manner proportional to the terrain mean complex reflectivity of $\sigma^0(x, y)$, which has an asymmetrical PDF and gamma distribution related to the phase, the amplitude, the intensity and the manner of the observation of the backscattered signal and the 2-D reconstructed image $I(x, y)$ [4]. In other words, the received backscattered signal is no longer a coherent signal, and any time the SAR collects the complex reflectivity values from the distributed point scatterers within a terrain, the HMN embedded within the signal has a constructive or destructive pattern and the pixel statistical distribution based on the amplitude, phase, and intensity will be affected. It should be noted that surfaces under the same amount of radiation and with similar texture would have different values of σ and produce different gray levels.

This noisy pattern of microwave imaging will be much more complicated when dealing with sea-ice terrains because of the complex electromagnetic interaction of different layers and the low backscattering profile of the sea-ice while being illuminated by active coherent radiation under different radiation scenarios [39]. Hence, an extended terrain backscattering modeling of the sea-ice on the basis of $\sigma^0(\cdot)$ might be helpful for further understanding of the presence of $N(t)$ within the backscattered signal as a major abnormal source of random pixels and the terrain electromagnetic interactions compared to previous works [26]–[41]. Accordingly, both the mean SAR image $I(\cdot)$ and the HMN spectrum follow from the hypothesis that the complex reflectivity $\sigma(\cdot)$ at different points at the same or at different times on the same terrain are uncorrelated. As a result, when addressing $\sigma(\cdot)$, the HMN manifests itself in the form of resolution cell disorders and SAR image pixel anomalies with statistical properties similar to those of thermal noise that make the raw data interpretation and texture analysis erroneous. Accordingly, the real reference SAR sea-ice image by KOMPSAT-5, as shown in Fig. 1, will be used for further profile investigations. As shown, the reference SAR sea-ice image includes open water and free floating snow surfaces such as sea-ice, ice floes and ice fragments, which differ on the basis of their shape, extent, thickness and concentration.

Accordingly, the contours of the sea-ice image vary in size, density and magnitude throughout the entire image, which is

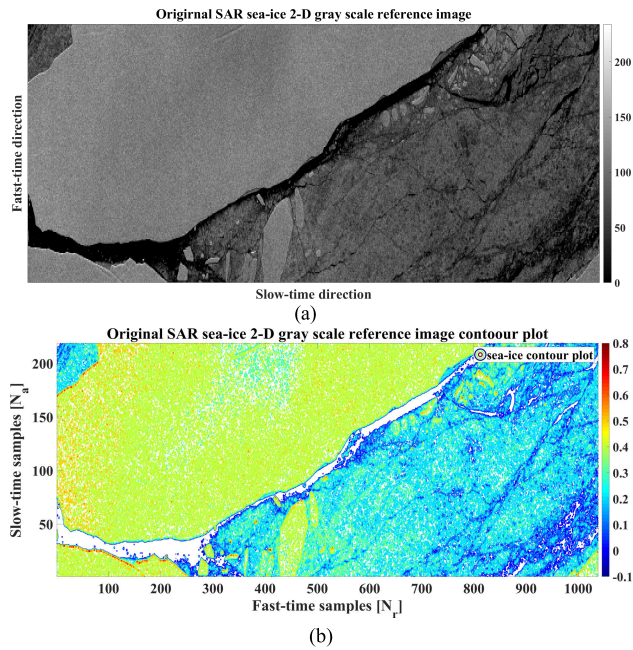


FIGURE 1. Original SAR sea-ice (a) reference image and (b) contour plot.

the result of backscattering coefficient alteration that presents as pixel anomalies among the adjacent resolution cells. This abrupt reflectivity alteration is a combined effect of the sensor and the sea-ice terrain interaction as the source of HMN that manifests as random pixel anomalies within the texture. Figs. 2 and 3 present a perspective of the aforementioned adverse HMN effects on the shape of pixel anomalies present and the suppressed scenario for comparison [4].

As can be deduced, the intensity alteration occurs both in the fast-time and slow-time directions between adjacent resolution pixels. From a backscattering point of view, each resolution cell contains several scattering centers with different complex reflectivity values whose electromagnetic interactions are influenced by the radiation scenario. According to the difference anomaly profile in Fig. 2(c) and 2(d), the abrupt intensity alterations have a higher rate in the fast-time direction and are more intense on the magnitude in the slow-time direction, which is the same of image frequency profile in Fig. 3. It is deduced that the adverse effects of HMN on the frequency profile can be more intense on the weaker signals with low signal-to-noise ratios (SNRs). The adverse HMN sensitivity presence can be observed from -8 dB to -14 dB with a difference magnitude of approximately 1 dB or 2 dB on the profile. These errors in the reception can present as pixel alterations, which are completely present in Fig. 4. As seen, an SNR deviation of 1 dB or 2 dB will result in a maximum pixel intensity alteration of 1 dB with a nonspecific pattern within the image.

As seen, an SNR deviation of 1 dB or 2 dB will result in a maximum pixel intensity alteration of 1 dB with a nonspecific pattern within the image. This pixel behavior is in the shape of random abrupt intensity changes or slow variations in

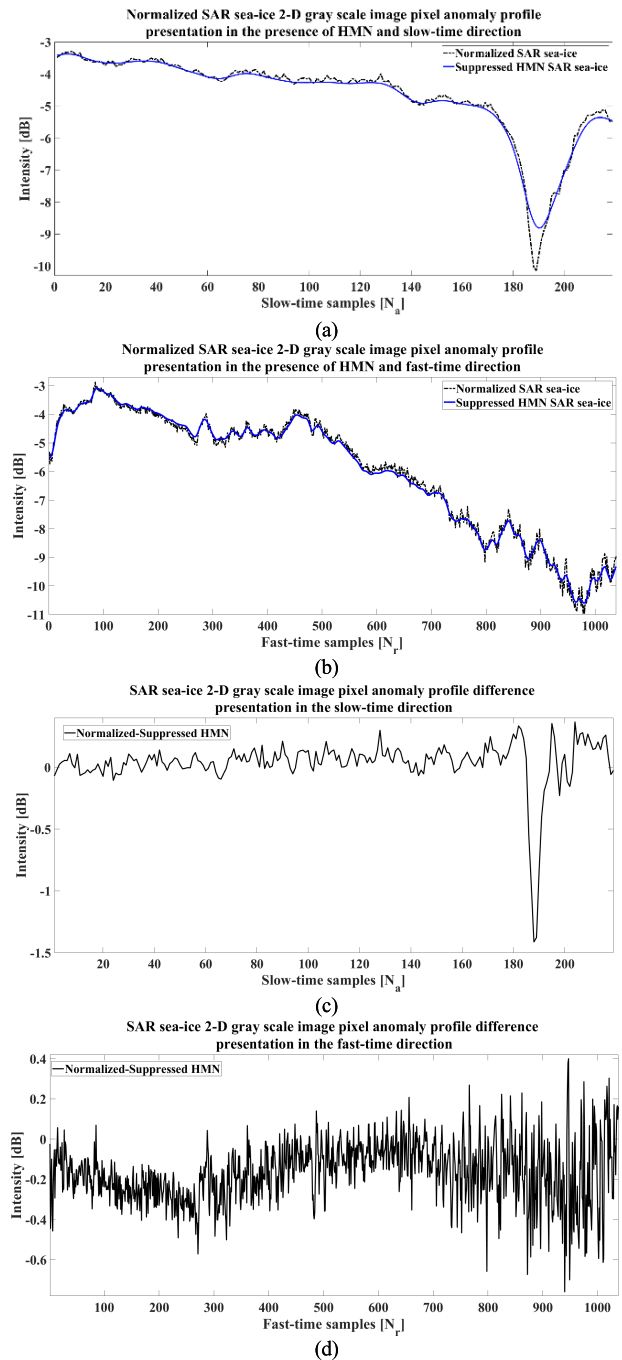


FIGURE 2. Normalized SAR sea-ice pixel anomaly profiles and comparisons: (a) slow-time direction, (b) fast-time direction, (c) slow-time direction difference profile, and (d) fast-time difference direction profile.

magnitude. The difference profiles in Figs. 2, 3 and 4 clearly show how HMN can degrade the SAR quality not only on the basis of raw data but also on the basis of images that are determined to occur due to electromagnetic interactions and texture behaviors.

Figures. 5 and 6 present the sea-ice pixel anomalies based on the gradient vector field (GVF) presentation. According to the GVF results in Fig. 5, the HMN adverse effects have

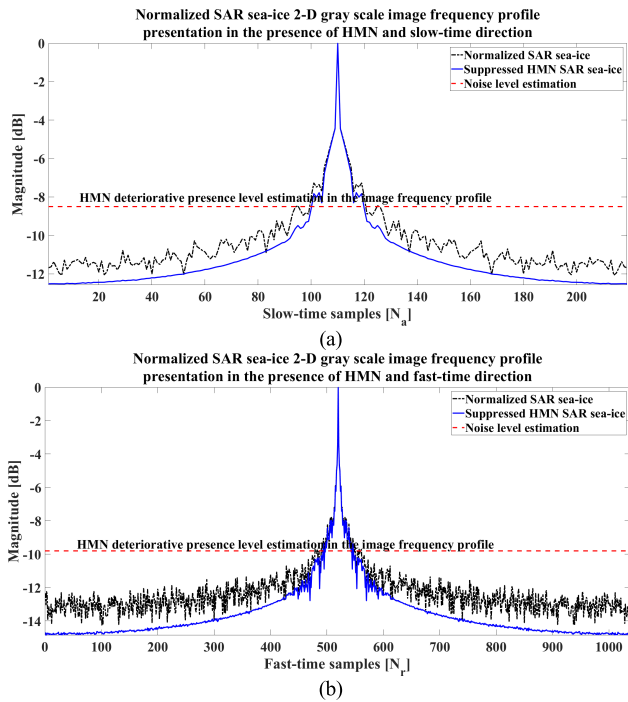


FIGURE 3. Normalized SAR sea-ice image frequency profile in the (a) slow-time direction and (b) fast-time direction.

a nonspecific pattern in the intensity anomaly, which causes the vector fields of the pixel components to be extended and less focused in both directions with a random distribution over the entire sea-ice terrain. It is also obvious that the main GVF concentrations are on the edges and boundaries due to their propagation model and pixel divergences. However, in ideal suppressed HMN conditions with less propagation disorder, the GVF concentration is supposed to be uniformly distributed and tends to be more focused, as shown in Fig. 6.

From a broader perspective, different texture states under a number of conditions occurring above and below the sea-ice terrain have their own direct influence on the coherence of the electromagnetic interactions and result in the source of uncorrelated HMN, which renders difficulties in the interpretation of the main features of SAR images in the form of pixel anomalies.

Accordingly, the local structural characteristics of the sea-ice pixel anomalies in Fig. 1 present the gradient maps of Fig. 7 and the kurtosis image of Fig. 8. The magnitude and direction maps in Figs. 7(a) and 7(b) are based on the intensity partial derivation along the fast-time and slow-time directions according to their quantized values, while the SAR kurtosis image in Fig. 8 is based on the probability distribution of the embedded HMN or the spatial interaction of adjacent pixel anomalies.

As seen in Figs. 7(a) and 8, specific regions are distinguished from the other homogenous regions because of the large gradient value and angle of probability as well as the tailedness of their distribution, which are more responsive to the sea-ice electromagnetic interactions. According to

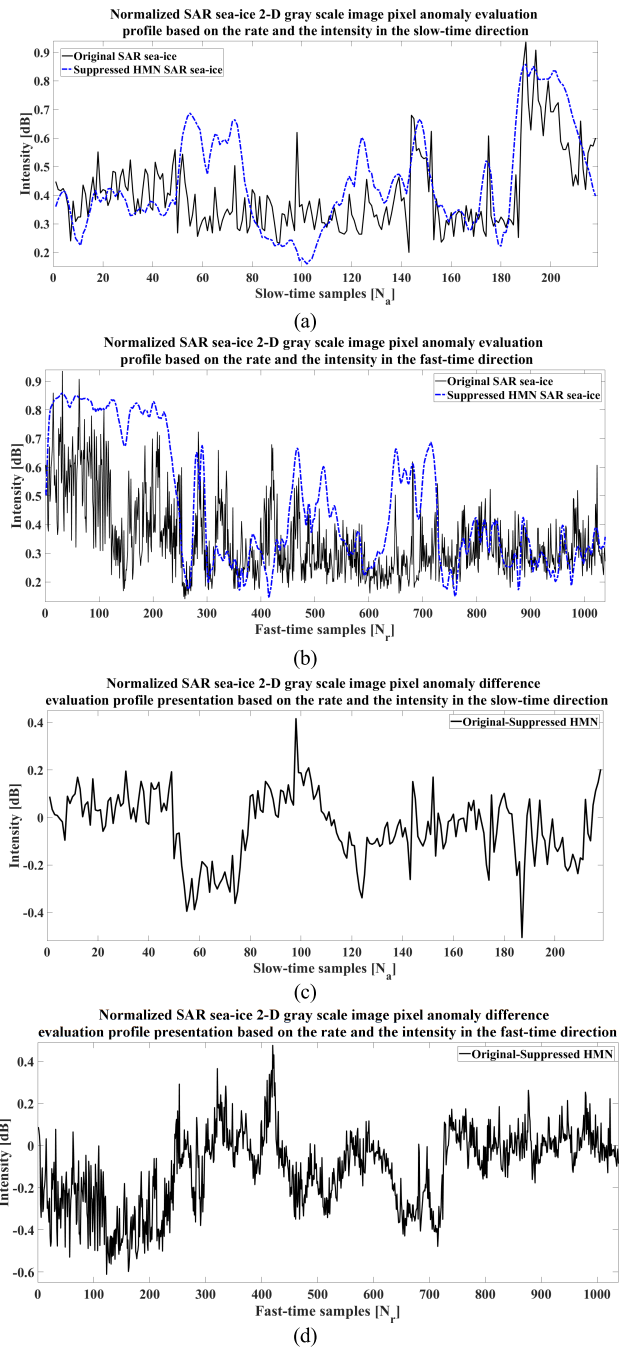


FIGURE 4. Normalized SAR sea-ice pixel anomaly evaluation based on the rate and intensity: (a) the slow-time direction, (b) the fast-time direction, (c) the slow-time difference direction profile, and (d) the fast-time difference direction profile.

Figs. 7(b) and 8, the presence of HMN will smooth the sea-ice image boundaries and lead to higher gradient map values and probability distributions, which makes it hard to distinguish the texture content known as an unstable area within the sea ice. According to Fig. 8, ice fragments, sea ice and edge boundaries are examples of unstable regions that produce pixel anomalies due to backscattering phenomena in the form of HMN behavior.

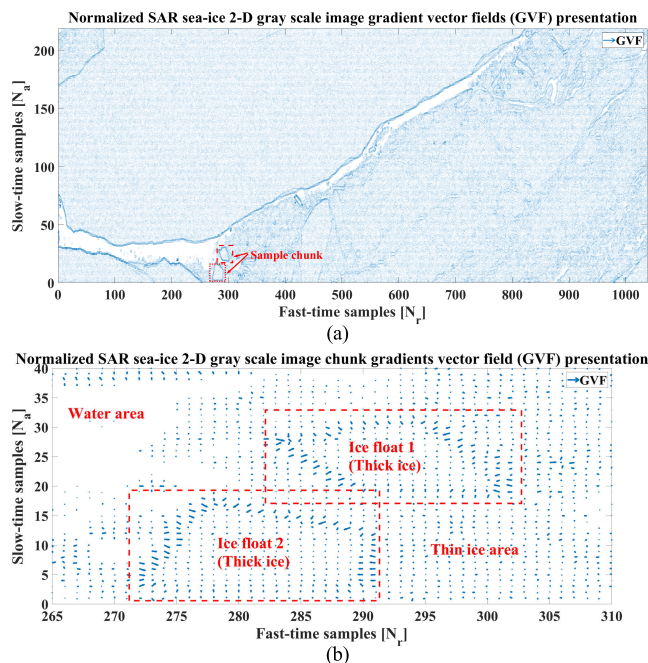


FIGURE 5. Normalized SAR sea-ice gradient vector fields: (a) the real size and (b) the zoomed-in view.

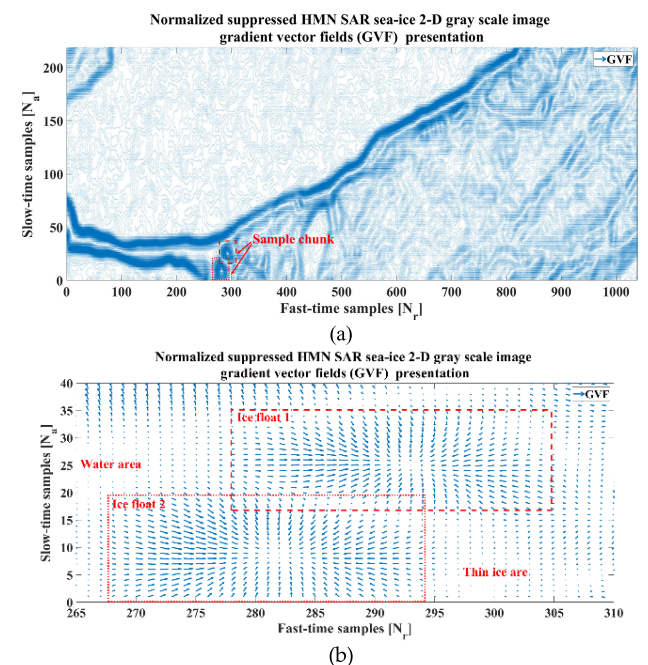


FIGURE 6. Suppressed HMN sea-ice gradient vector field (a) the real size and (b) the zoomed-in view.

In short, the HMN has a random distribution with a nonspecific pattern of pixel anomalies and does not follow a spatial variation related to the average reflectivity of the illuminated terrain. Hence, in addition to image resolution profile extraction, a spatial resolution profile analysis based on distributed scatterer reflectivity measurements might help to investigate SAR sea-ice electromagnetic interaction behaviors. In other

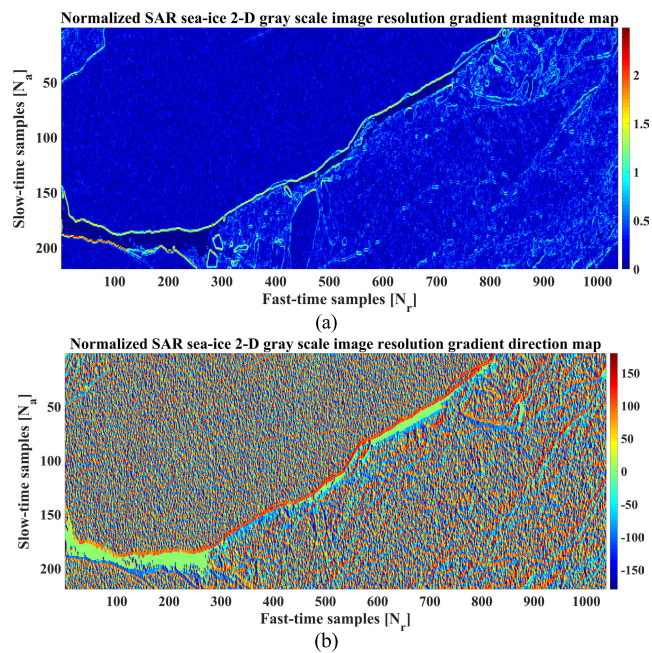


FIGURE 7. Normalized SAR sea-ice image resolution gradient map (a) the gradient magnitude and (b) the gradient direction.

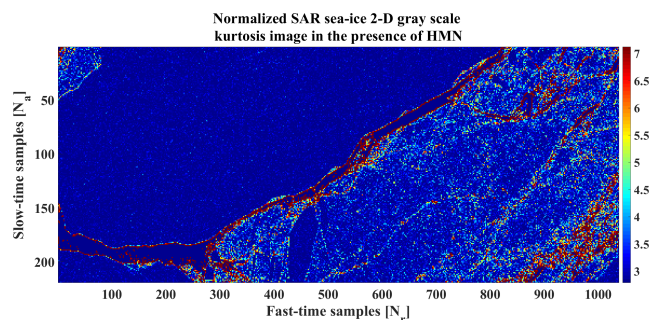


FIGURE 8. Normalized SAR sea-ice kurtosis.

words, distinguishing features of the sea-ice texture, such as the edge sharpness, extent, volume, and roughness, as key descriptors of sea-ice are the source of the random distribution of HMN in the shape of pixel anomalies.

Therefore, it is necessary to investigate the uncorrelated interaction of sea ice on the basis of active sensor-terrain spatial resolution profile extraction. In comparison to the image resolution evaluations in Figs. 2 to 8, the sea-ice spatial resolution is not only dependent on the electromagnetic interaction phenomena but also relies on sensor parameters such as the carrier frequency and observation time. However, the results of the noncoherent electromagnetic interaction evaluation are not parameter oriented. In other words, when the received backscattered data are extracted, the effects of the sensor parameters will not change the randomness of the HMN but are necessary for such spatial profile extraction. It should be noted that, compared to the evaluation of the image pixel resolution, which is intensity oriented, the evaluation of the spatial resolution is based on the spatial

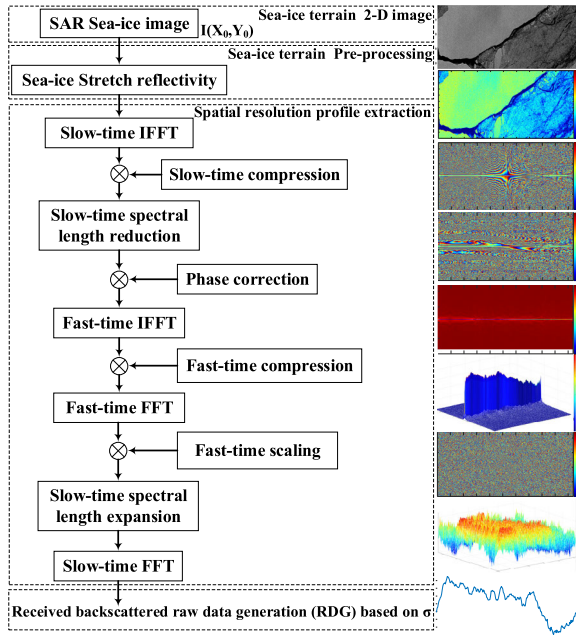


FIGURE 9. Sea-ice spatial resolution and backscattered data profile extraction algorithm.

TABLE 1. Main parameters of the SAR sensor.

Parameter	Value
Carrier frequency	10 GHz
Repetition frequency	5 KHz
Sampling frequency	180 MHz
Pulse width	0.8 μsec
Bandwidth	190 MHz
Chirp scaling factor	1

configurations of sensor-terrain active interactions in the form of front-end phase history analysis. In this paper, the extraction of the received backscattered data profile is carried out on the basis of time-frequency domain IFA according to Table 1 and the RDG routines of Fig. 9 [4].

The purpose of SAR spatial resolution analysis is twofold. The first, namely, the extraction of raw data, allows the evaluation of the adverse effects of HMN on the active interaction behavior of the texture while it is being backscattered to the sensor in the form of raw data. The second is the detection of unstable regions as a source of anomalies. Referring to the proposed RDG method in Fig. 9, the incoherent information of the reference SAR sea-ice image will be first imported to a preprocessing step on the supposition of a non-backscattered background, which is called surface reflectivity stretching. Terrain reflectivity stretching makes the sea-ice texture homogenous for spatial resolution profile extraction. It should be noted that the selection of the sensor parameters for the algorithm is dependent on the size of the reference image. Accordingly, the result in Fig. 10 shows the extracted normalized SAR sea-ice received

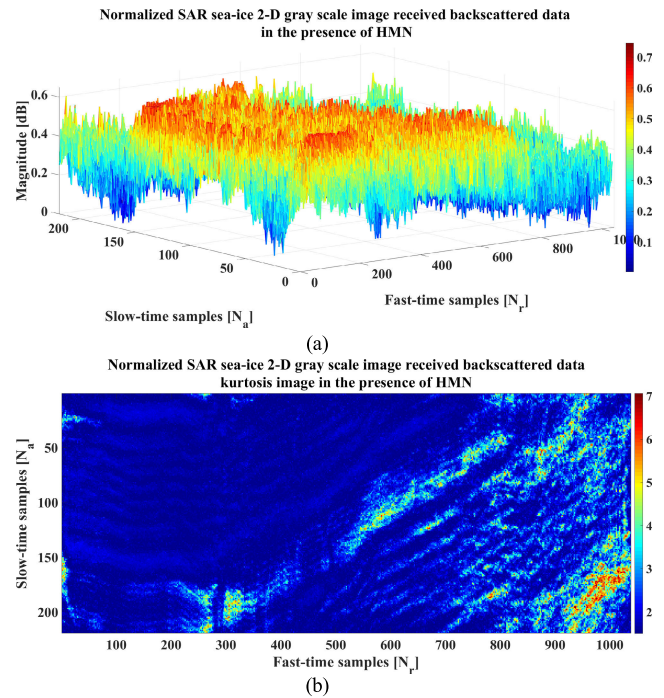


FIGURE 10. Normalized SAR sea-ice received backscattered data (a) 3-D view and (b) kurtosis image.

backscattered data as well as its kurtosis image. As can be deduced, the maximum backscattered magnitude of the terrain-sensor interaction is approximately 0.75 dB, while the minimum is approximately 0.35 dB. In other words, the thick homogenous sea-ice floe has stronger complex reflectivity magnitudes; as the texture changes to ice fragments, including drifted thin ice sheets and sea-ice, the magnitude decreases. Figure.10(b), which is the same as Fig. 8, presents the kurtosis image of the received backscattered data from Fig. 10(a).

According to the results, the sea-ice section including open water and ice fragments presents higher random noise sparsity relative to the HMN distribution. In other words, the peak values in the kurtosis image indicate the direction and severity of the HMN, as sign of pixel anomaly within the sea-ice. The higher the kurtosis of the raw data, the more resolution cells that will have the dominant HMN level; however, a uniform distribution of kurtosis is an extreme case that will not happen in real RDG. In the same way, Figs. 11(a) and 11(b) present a complete perspective of the reflectivity alteration and HMN sparsity in the reference KOMPSAT-5 sea-ice image while being overlaid. As seen, the sea-ice texture including open water and thinner ice fragments are the most likely sources of pixel anomalies, which has also been shown in Figs. 8 and 10(a).

As a result, the probability distribution of the HMN over the sea-ice texture is peaked and flat relative to the spatial configuration of the uncorrelated source of pixel anomalies, which are more likely to occur in areas with open water, ice fragments, drifted particles and mixed sea-ice textures.

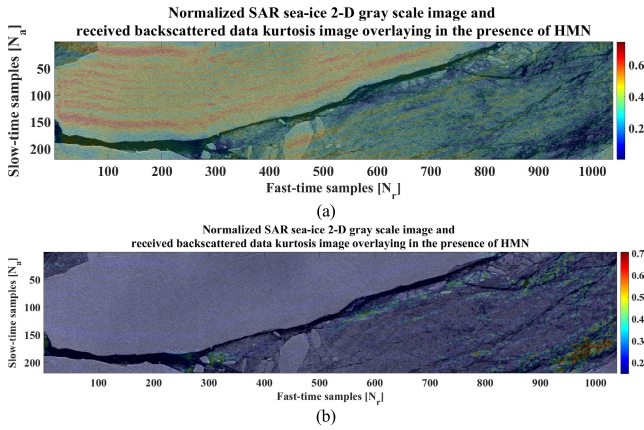


FIGURE 11. Normalized SAR sea-ice overlaying image with (a) the received backscattered data image and (b) the received backscattered data kurtosis image.

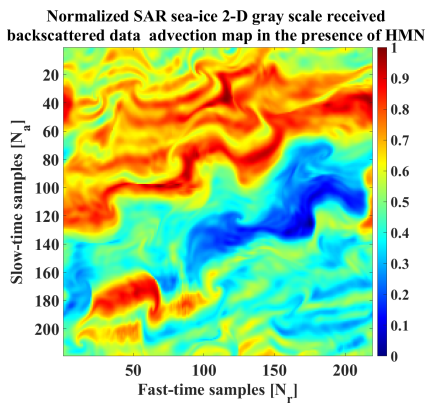


FIGURE 12. Normalized SAR sea-ice received backscattered data advection map.

Figure 12 presents the aforementioned results on the basis of the advection map of the sea-ice RDG according to the external vector field approximation of reflectivity distributions in Fig. 10(a). Due to the dynamic coherent features of electromagnetic propagation, it is observed that thick ice floes and the fragmented ice have dense spatial representation of the vector fields within their spatial resolution cells in comparison to other reflectivities. The received backscattered sea ice signals are diffused to neighboring regions of vector fields that can be used for sea-ice complex RDG prediction and pixel anomaly studies while dealing with HMN spatial resolution analysis.

Accordingly, the results in Fig. 13 present the adverse effects of HMN on the sensor-terrain spatial resolution. It is shown that the deteriorative effects of HMN on the spatial resolution in the fast-time direction have a much faster rate rather than the slow-time direction; however, it has almost the same pea-to-peak magnitude of alteration, which is approximately 1 dB as in the image resolution in Fig. 4. Similar to the results of the image resolution in Figs. 2 and 4, the HMN in both directions is observed as destructive but with different rates and magnitudes.

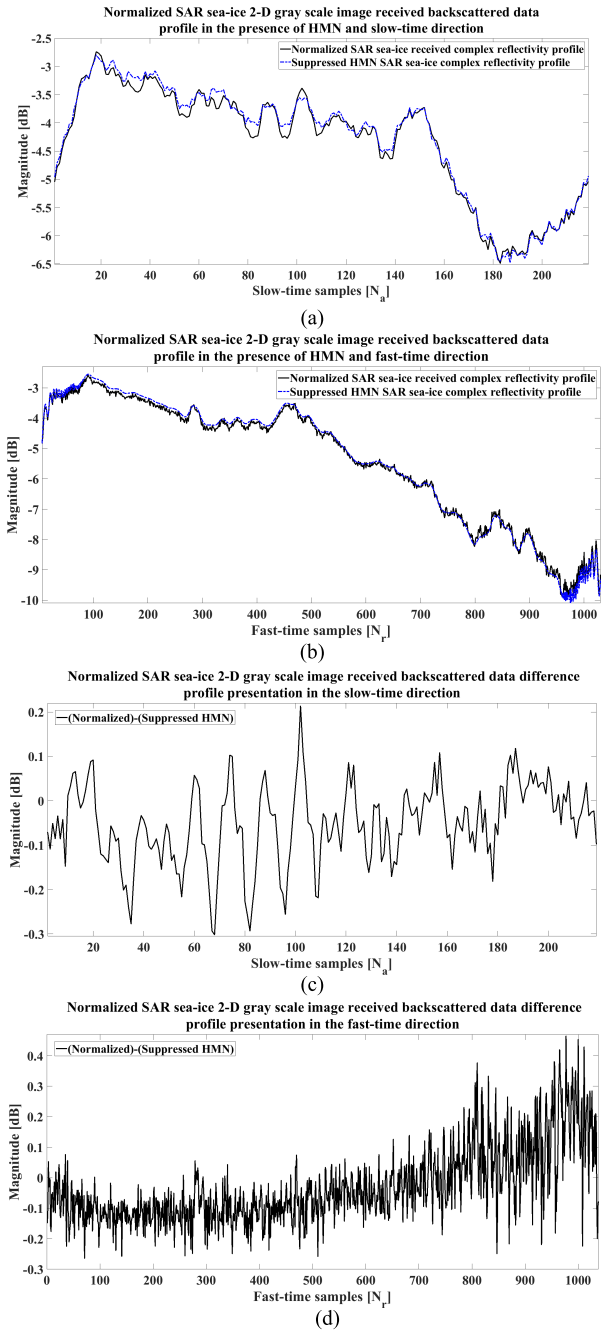


FIGURE 13. Normalized SAR sea-ice spatial resolution profile presentation and comparison: (a) slow-time direction, (b) fast-time direction, (c) slow-time direction difference profile, and (d) fast-time difference direction profile.

In comparison to the spatial resolution, the image resolution is more sensitive to the presence of HMN, and the slow-time direction is more sensitive to HMN than the fast-time direction. In general, HMN is multiplicative, and increasing the transmit signal power will not reduce the HMN level because the variance increases with the intensity. Likewise, improving the signal bandwidth for fine-range resolution will result in a high data rate with the computational cost in the fast-time direction and increase the chance of the

presence of HMN. In the slow-time direction, the situation is more complex due to the interrelations between various sensor parameters and the resolution. As a result, HMN tends to weaken for very high-resolution systems, since the number of elemental scatterers within a resolution cell decreases.

It is worth noting that the information capacity per resolution cell is very small, and consequently, the complete removal of HMN and normally pixel anomaly correction is impossible without sacrificing the resolution [42]. As a key descriptor, HMN and pixel anomaly correction based on the HMN distribution model still remain. In short, the HMN distribution model within the SAR sea-ice texture play a key role in the qualitative and quantitative assessment of verification scenarios. The next section will provide more details on the modeling, removal and evaluation analysis.

B. KOMPSAT-5 SAR SEA-ICE HMN SUPPRESSION, HMN DISTRIBUTION FORMULATION AND TEXTURE CLASSIFICATION APPROACH

Since sea-ice regions are often difficult to access, in situ metrics to validate calculated SAR results are sparse. On the other hand, the presence of HMN in SAR images reduces the accuracy of the texture analysis on the basis of electromagnetic interactions. Thus, it is important to address the SAR sea-ice texture in a way not only capable of reducing the adverse effects of the HMN but also able to improve the possibility of texture specification with minimal loss of information. Hence, this section will briefly introduce the approach to KOMPSAT-5 SAR sea-ice HMN suppression based on the TFD technique, HMN spectral property formulation and texture classification. The concept of HMN suppression and spectral formulation is based on the DWT decomposition method, while the classification is proposed on the basis of two separate iterative and adaptive K-means clustering algorithms.

1) SAR HMN SUPPRESSION BASED ON A TEXTURE DECOMPOSITION APPROACH

The major disadvantage of the methods used in SAR sea-ice texture analysis is the application of joint probability distributions of the pixels based on a single scale. In other words, such methods share one common weakness, that is, the focus on the coupling between image pixels on a specific scale while completely ignoring the adverse effects of the presence of HMN in the shape of pixel anomalies when dealing with 2-D received backscattered data. Hence, the need for a method that represents the 2-D SAR sea-ice grayscale image in a domain whose coordinate system has an interpretation closely related to the characteristics of the texture, such as the frequency, time, and intensity, is very important to characterize effectively the adverse effects of pixel anomalies and HMN at different scales of the texture. As previously introduced, the DWT is a formal, unified multiresolution TFD framework for multiscale decomposition of 2-D images, which can help to retrieve the SAR sea-ice texture contents based on maximizing the recognition rate while capturing

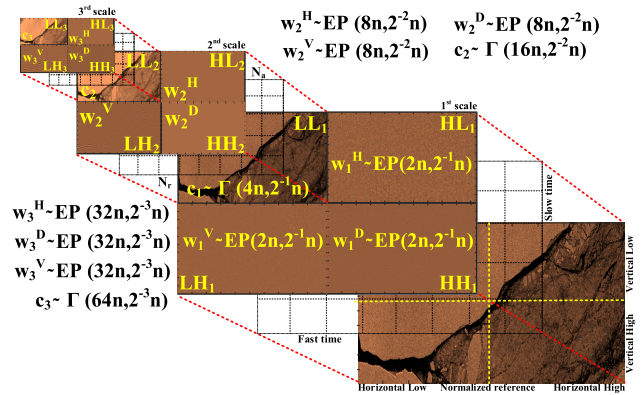


FIGURE 14. Normalized SAR sea-ice multiresolution and multiscale DWT decomposition and PDF property coefficients for the HMN intensity.

the distribution information of the texture at different coordinates. The 1-D DWT algorithm can be extended to a 2-D DWT by the tensor product of two 1-D wavelets along the horizontal and vertical directions with some geometric and frame arrangement definitions, as shown by (2) [33], [43]. At each scale, the decomposition scheme applies the scaling filter and the wavelet filter alternately to the columns and rows of the 2-D image under TFD analysis. At any decomposition level $l = 1, \dots, L$, according to their frequency components, the input is transformed into four subbands. They are called the approximated subband LL and the other three detailed subbands are HL , LH and HH , while L is the result of low-pass scaling filtering and H is for high-pass wavelet filter. Since the approximation of subband LL at any scale contains any low-frequency components of the reference image, it carries most of the original information, whereas the detailed subbands HL , LH and HH capture the horizontal, vertical, and diagonal features, respectively. Subband LL will be used as an input for further scale decomposition in the case of multiscale analysis at level $l + 1$. At scale 0, LL is represented by the reference image. Hence, the scaled and translated basis elements of the 2-D DWT algorithm are as follows:

$$\begin{aligned}
 LL &= c(x, y) = c(x)c(y) \\
 HL &= w^H(x, y) = w(x)c(y) \\
 LH &= w^V(x, y) = c(x)w(y) \\
 HH &= w^D(x, y) = w(x)w(y)
 \end{aligned} \tag{2}$$

where, $c(x, y)$ is the scaling function, $w(x, y)$ is the wavelet function, the superscripts H , V and D refer to the decomposition direction of the wavelet, which are used as part of 2-D image manipulation, while the multiresolution representation of scaling is given by (3) and Fig. 14:

$$\begin{aligned}
 c_{l,m,n}(x, y) &= 2^{\frac{l}{2}} c(2^l x - m, 2^l y - n) \\
 w_{l,m,n}^k(x, y) &= 2^{\frac{l}{2}} w(2^l x - m, 2^l y - n) \quad \text{where } k = \{H, V, D\}
 \end{aligned} \tag{3}$$

In the case of 2-D SAR sea-ice image decomposition according to (1) and with the help of (2), the DWT function of SAR image with sizes N_a and N_r on the basis of the scaling function and its corresponding wavelet functions are defined as:

$$\begin{aligned}
 T_c(l_0, m, n) &= \frac{1}{\sqrt{N_a N_r}} \sum_{x=0}^{N_a-1} \sum_{y=0}^{N_r-1} I(x, y) c_{l_0, m, n}(x, y) \\
 T_w^H(l, m, n) &= \frac{1}{\sqrt{N_a N_r}} \sum_{x=0}^{N_a-1} \sum_{y=0}^{N_r-1} I(x, y) w_{l, m, n}^H(x, y) \\
 T_w^V(l, m, n) &= \frac{1}{\sqrt{N_a N_r}} \sum_{x=0}^{N_a-1} \sum_{y=0}^{N_r-1} I(x, y) w_{l, m, n}^V(x, y) \\
 T_w^D(l, m, n) &= \frac{1}{\sqrt{N_a N_r}} \sum_{x=0}^{N_a-1} \sum_{y=0}^{N_r-1} I(x, y) w_{l, m, n}^D(x, y)
 \end{aligned} \tag{4}$$

where $T_c(\cdot)$ is the scaling function and $T_w^H(\cdot)$, $T_w^V(\cdot)$ and $T_w^D(\cdot)$ are the horizontal subband, vertical subband and diagonal subband representations, respectively, of the SAR sea-ice image. It should be noted that the inverse DWT of the aforementioned decomposition is derived as (5):

$$\begin{aligned}
 I(x, y) &= \frac{1}{\sqrt{N_a N_r}} \sum_m \sum_n T_c(l_0, m, n) c_{l_0, m, n}(x, y) \\
 &+ \frac{1}{\sqrt{N_a N_r}} \sum_{l=H, V, D} \sum_{l=l_0} \sum_m \sum_n \\
 &\times T_w^k(l, m, n) w_{l, m, n}^k(x, y)
 \end{aligned} \tag{5}$$

According to the above formulation, the DWT decomposition method is used to transform 2-D images into representations in which both the SAR spatial and frequency information are presented within different scales that are easy to interpret. Accordingly, every subband image contains information on a specific scale and orientation, which are conveniently separated while their spatial information is retained within the subimages. Therefore, extracting the subimage information based on the embedded properties might be helpful. The spectral properties are one of the characteristics that are important to extract for KOMPSAT-5 SAR analysis. Spectral property extraction, specifically the HMN spectral formulation, will be described in the next section.

2) SAR HMN PROPERTY FORMULATION BASED ON THE DWT DECOMPOSITION APPROACH

As described previously, due to the different physical properties of the complex sea-ice terrain illuminated by incidental electromagnetic waves, the independent point scatterers within resolution cells will generate random coherent interferences in the form of HMN in sea-ice images.

The characteristics of the HMN are very important, and they differ from those found in other sensors, such as their coherency, the multiplicative behavior, the asymmetrical PDF, the distribution model and the dependency on the backscattered signal that is completely under the control of phase, amplitude and intensity distribution of the observation mode. In other words, as the reference image is decomposed

into further scales, the HMN will be changed based on the expectation and the variance of the SAR sea-ice coefficients, which will be modulated by the characteristics of the HMN proportional to the texture mean backscattering. In short, despite the limitation of the random sea-ice propagation, when the 2-D image is being decomposed, HMN property extraction is not only possible but also helps for profile evaluation, which provides a complete statistical presentation of the HMN coefficients. According to (1) and for the purpose of statistical analysis of the HMN, let us consider the SAR sea-ice observations, which will be mapped in two dimensions (6):

$$P = I_S \cdot N \tag{6}$$

where P is the SAR observed pixel, I_S is the average sea-ice pixel intensity, and N is the HMN intensity. I_S and N are considered two independent random variables within the image pixels. P_1 and P_2 are considered two adjacent pixels in a SAR observation:

$$\begin{aligned}
 P_1 &= \alpha N_1 \\
 P_2 &= \beta N_2
 \end{aligned} \tag{7}$$

where α and β are constants and N_1 and N_2 are independent HMN random variables with identical PDFs according to the general gamma distribution $\Gamma(n, \lambda)$ as in (8):

$$p(N) = \frac{\lambda^n}{(n-1)!} N^{n-1} \exp(-\lambda N) \tag{8}$$

where N is the result of HMN components that are observed with a specific phase and amplitude, as derived in (1). Moreover, P_1 and P_2 can be modeled as two adjacent pixels in an observation of P , where α and β are the pixel intensities. In the case of $\alpha = \beta$, the two adjacent pixels P_1 and P_2 belong to a homogenous region. Otherwise, P_1 and P_2 are located in two different regions. If $\alpha \neq 0$ and $\beta \neq 0$, P_1 and P_2 follow the general gamma distribution with the form of (9):

$$\begin{aligned}
 p_{P_1}(N) &= \frac{\lambda^n}{\alpha (n-1)!} \left(\frac{N}{\alpha}\right)^{n-1} \\
 &\exp\left(\frac{-\lambda}{\alpha} N\right) \quad \text{where } N, n \geq 0, \text{ and} \\
 p_{P_2}(N) &= \frac{\lambda^n}{\beta (n-1)!} \left(\frac{N}{\beta}\right)^{n-1} \exp\left(\frac{-\lambda}{\beta} N\right) \quad \text{where } N, n \geq 0
 \end{aligned} \tag{9}$$

The property of $P_1 - P_2$ is the basis for the development of HMN properties and coherent complex modeling in the 2-D DWT domain. Hence, if the cumulative distribution function of $P_1 - P_2$ is defined as:

$$P(P_1 - P_2 < t) = \iint_{N \leq t} p_{P_1}(N) p_{P_2}(N) dN \tag{10}$$

then the following will result (11), as shown at the bottom of the next page.

The PDF of $P_1 - P_2$ can be derived as:

$$p_{P_1-P_2}(N) = \frac{\exp\left(-\frac{\lambda}{\beta}|N|\right)}{(n-1)!} \left(\frac{\lambda}{\alpha}\right)^n \left(\frac{\lambda}{\beta}\right)^n \left[\sum_{j=0}^{n-1} \frac{(n+j-1)!}{j!(n-j-1)!\left(\frac{\lambda}{\alpha} + \frac{\lambda}{\beta}\right)^{n+j}} |N|^{n-j-1} \right] \quad (12)$$

Hence, the moments of $P_1 - P_2$ can be derived by:

$$E[N^i] = \frac{2}{(n-1)!} \left(\frac{\lambda}{\alpha}\right)^n \left(\frac{\lambda}{\beta}\right)^n \left[\sum_{j=0}^{n-1} \frac{(n+j-1)!(i+n-j-1)!}{j!(n-j-1)!\left(\frac{\lambda}{\alpha} + \frac{\lambda}{\beta}\right)^{n+j}} \left|\frac{\beta}{\lambda}\right|^{i+n-j} \right]$$

$$E[N^i] = 0 \quad \begin{array}{l} \text{if } i \text{ is even} \\ \text{if } i \text{ is odd} \end{array} \quad (13)$$

For the purpose of HMN complex behavioral modeling, let $\alpha = \beta = 1$. Hence, (12) can be rewritten as:

$$p_{P_1-P_2}(N) = \frac{\exp(-\lambda|N|)}{(n-1)!} (\lambda)^{2n} \times \left[\sum_{j=0}^{n-1} \frac{(n+j-1)!}{j!(n-j-1)!(2\lambda)^{n+j}} |N|^{n-j-1} \right] \quad (14)$$

Equation (14) is the combination of exponential and polynomial functions, and if a random variable follows the abovementioned function, it follows an exponential polynomial (EP) distribution and can be stated as an EP(n, λ) distribution. Accordingly, the EP distribution and its corresponding statistical features are the basis of HMN behavioral analysis in TFD. Suppose $\{P_i\}$ is an observed set of HMN data with independent variables that follow a gamma distribution $\Gamma(n)$. To the best of our knowledge, if $\lambda = n$, the general distribution of $\Gamma(n, \lambda)$ is simplified to $\Gamma(n)$. After a 1-D DWT using Haar's mother wavelet, the result would be as follows:

$$T_1^1([P_1, P_2]) = [c_{11}, w_{11}] = \frac{1}{\sqrt{2}}[P_1 + P_2, P_1 - P_2] \quad (15)$$

where c_{11} is the scaling coefficient (SC) in the low-pass filtering direction and w_{11} is the discrete wavelet coefficient (DC) in high-pass filtering, which are independent variables of the HMN. All the SCs follow a general gamma distribution, while the DCs follow an EP distribution. In the

case of two-scale 1-D DWT decomposition, (15) can be rewritten as:

$$T_2^1([P_1, P_2, P_3, P_4]) = [c_1, w_{21}, w_{11}, w_{12}]$$

$$= \frac{1}{2}[P_1 + P_2 + P_3 + P_4, P_1 + P_2 - P_3 - P_4, P_1 - P_2, P_3 - P_4] \quad (16)$$

Similarly, for M-scale 1-D DWT decomposition, the PDFs of the SCs and DCs follow the gamma distribution and EP distribution, respectively, as below:

$$c_M \sim \Gamma(2^M n, 2^{-M/2} n)$$

$$w_M \sim EP(2^{M-1} n, 2^{-M/2} n) \quad (17)$$

In the case of 2-D DWT decomposition, the abovementioned result can be generalized. Suppose $\bar{P} = \{P_{i,j}\}_{0 \leq i,j < n}$ is a homogenous region with unitary backscatter intensity, as shown in (6). $\{P_{i,j}\}$ are independent HMN random variables with the gamma distribution $P_{i,j} \sim \Gamma(n)$. The behavior of HMN in the DWT domain has two parts (scaling and wavelet coefficients), and every SC and DC depend on a $2^M \times 2^M$ block in the normalized reference image after M-scale DWT decomposition. According to one-scale DWT decomposition in (16):

$$W^1 \left(\begin{bmatrix} P_{11} & P_{12} \\ P_{21} & P_{22} \end{bmatrix} \right) = \begin{bmatrix} c_1 & w_1^H \\ w_1^V & w_1^D \end{bmatrix}$$

$$= \frac{1}{2} \begin{bmatrix} P_{11} + P_{12} + P_{21} + P_{22} & P_{11} - P_{12} + P_{21} - P_{22} \\ P_{11} + P_{12} - P_{21} - P_{22} & P_{11} - P_{12} - P_{21} + P_{22} \end{bmatrix} \quad (18)$$

Based on (18), the following result can be derived:

$$c_1 \sim \Gamma(4n, \frac{1}{2}n)$$

$$w_1^i \sim EP\left(2n, \frac{1}{2}n\right), \quad i = H, V, D \quad (19)$$

After an M-scale DWT decomposition, (19) can be rewritten as:

$$c_M \sim \Gamma(4^M n, 2^{-M}n)$$

$$w_M^i \sim EP(2^{2M-1} n, 2^{-M}n) \quad (20)$$

Figure 14 shows the PDF of the HMN intensity for every SC and DC in the case of three-scale SAR sea-ice image decomposition. According to the above TFD distribution modeling of HMN based on DWT, PSD modeling is considered the best possible option to investigate the adverse effects of HMN within KOMPSAT-5 SAR sea-ice images. The PSD is an objective quality assessment metric that measures the intensity of the joint pixels as a function of the frequency

$$P(P_1 - P_2 < t) = \begin{cases} \frac{\exp\left(-\frac{\lambda}{\beta}|t|\right) \frac{\lambda^n}{\alpha^n(n-1)!} \sum_{i=0}^{n-1} \frac{\lambda^i}{\beta^i} \left[\sum_{j=0}^i \frac{|t|^{i-j}}{j!(i-j)!} \frac{(n+j-1)!}{\left(\frac{\lambda}{\alpha} + \frac{\lambda}{\beta}\right)^{n+j}} \right]}{1 - \exp\left(-\frac{\lambda}{\beta}|t|\right) \frac{\lambda^n}{\alpha^n(n-1)!} \sum_{i=0}^{n-1} \frac{\lambda^i}{\beta^i} \left[\sum_{j=0}^i \frac{|t|^{i-j}}{j!(i-j)!} \frac{(n+j-1)!}{\left(\frac{\lambda}{\alpha} + \frac{\lambda}{\beta}\right)^{n+j}} \right]} & t \leq 0 \\ 1 - \exp\left(-\frac{\lambda}{\beta}|t|\right) \frac{\lambda^n}{\alpha^n(n-1)!} \sum_{i=0}^{n-1} \frac{\lambda^i}{\beta^i} \left[\sum_{j=0}^i \frac{|t|^{i-j}}{j!(i-j)!} \frac{(n+j-1)!}{\left(\frac{\lambda}{\alpha} + \frac{\lambda}{\beta}\right)^{n+j}} \right]} & t > 0 \end{cases} \quad (11)$$

and shows at which frequencies the intensity variations are strong and at which frequencies the intensity variations are weak. According to the above model, pixel anomalies and their statistical distribution based on amplitude, phase and intensity play a key role in complex PSD simulation. The results after HMN suppression and modeling will be used not only for classification but for objective verification. In short, the essence of HMN suppression using DWT analysis is to reduce the HMN level in the TFD, while our primary objective is to focus on PSD function modeling and prepare the image for postprocessing tasks, such as segmentation and classification.

3) SAR UNSUPERVISED TEXTURE SEGMENTATION BASED ON THE K-MEANS CLASSIFICATION APPROACH

The sea-ice image reconstruction consists of numerous microwave interactions, intermodulation processes, propagation and backscattering effects based on random complex structures. Due to the inherent SAR pixel anomaly presence, sea-ice pixel-oriented spatial information extraction remains a challenging task. On the other hand, sea-ice local feature extraction is a translational variant, which is a problem for the segmentation of homogenous textured images. Hence, it can be advantageous to include spatial information in the feature sets of segmentation not only to increase the pixel information accuracy but also to reduce misinterpretations. As described previously, hierarchical DWT texture decomposition has the ability to suppress the adverse effects of HMN and incorporate contextual information in the case of pixel anomaly correction. It should be noted that the reconstructed images are the same size as the normalized reference image, so that no components will artificially dominate the classification problem, which is an issue that commonly occurs with segmentation algorithms.

Accordingly, subband multiresolution image segmentation will be applied according to the decomposition scale. The above considerations suggest associating an unsupervised classification method that uses the generated features with a class label according to their position in the sea-ice feature space. The K-means clustering algorithm is a deterministic routine that aims to divide several observations into user-defined classes where each observation only belongs to one class with the class centroid nearest to the observation. The basic idea of the K-means is to cluster the closest samples by in K groups. Iteratively, the values of the centroids of the clusters are updated one by one until the best clustering results are obtained on the basis of a criteria function. The adjustment criteria of the iterations are obtained by finding the values of objective function. The K-means considers the distance as the similarity index to find the optimal classification so that the objective index is minimized. The value of K should be given in advance, and the selection of the K is based on prior supervised information.

In this research, the main idea of K-means clustering is proposed based on two separate simultaneous algorithm implementations for the purpose of further verifications.

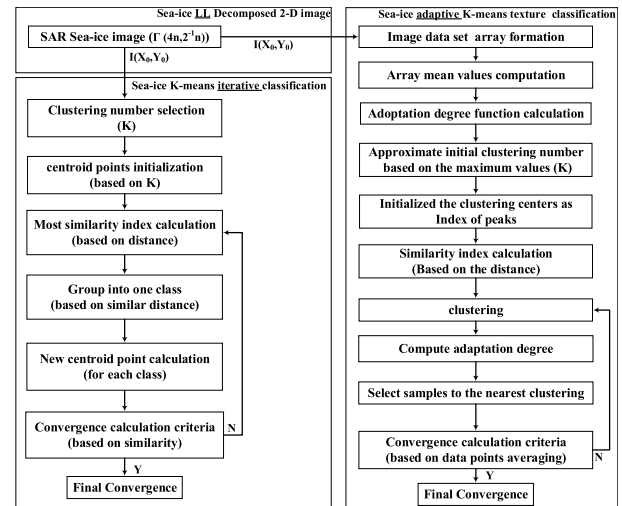


FIGURE 15. Normalized SAR sea-ice K-means texture classification procedure including normal iterative and adaptive clustering.

First, the K-means SAR sea-ice image classification is tuned and applied directly on the decomposed sea-ice image based on the iterative mode. Second, the K-means clustering algorithm classifies the decomposed SAR sea-ice image on the basis of adaptive mode. Both algorithms are the same in terms of their purpose (classification), but in adaptive mode, the number of K results based on recursive adaptive training of the algorithm and is not known in advance. Figure 15 shows both proposed K-means classification algorithms in detail. According to Fig. 15, the feature vector descriptions are based on the normalized column pixel values that can be grouped in white, light gray, gray, dark and black pixels, which are defined on the basis of KOMPSAT-5 sea-ice image maximum value and are known as clustering number. After pixel conversion into column vectors, the algorithm should find the centroid of each clusters for minimization of the index criteria. The centroid points initialization is calculated on the basis of averaging the sea-ice image maximum value on the basis of clustering number where each point corresponds to one segment. Next, the samples are grouped into segments based on the similarity index. Here, the similarity is computed as the distance value between one iteration and the centroid point. In other words, the samples goes to the segment with the most similarity.

After all of the samples have been assigned to one segment, the new centroid points in each specific segment are calculated again. Then, each sample finds its cluster with the criterion of most similarity in the next iteration. This procedure is repeated until all of the centroid points converge. On the other hand, in the adaptive clustering algorithm, there are some differences in the adaptation, segmentation number selection, centroid initialization, criteria calculation and convergence routine. In the adaptive K-means, the convergence of the model is based on external neighbor segments and the mean gray-level value computation while in the iterative mode, it is performed inside the segments and with the help

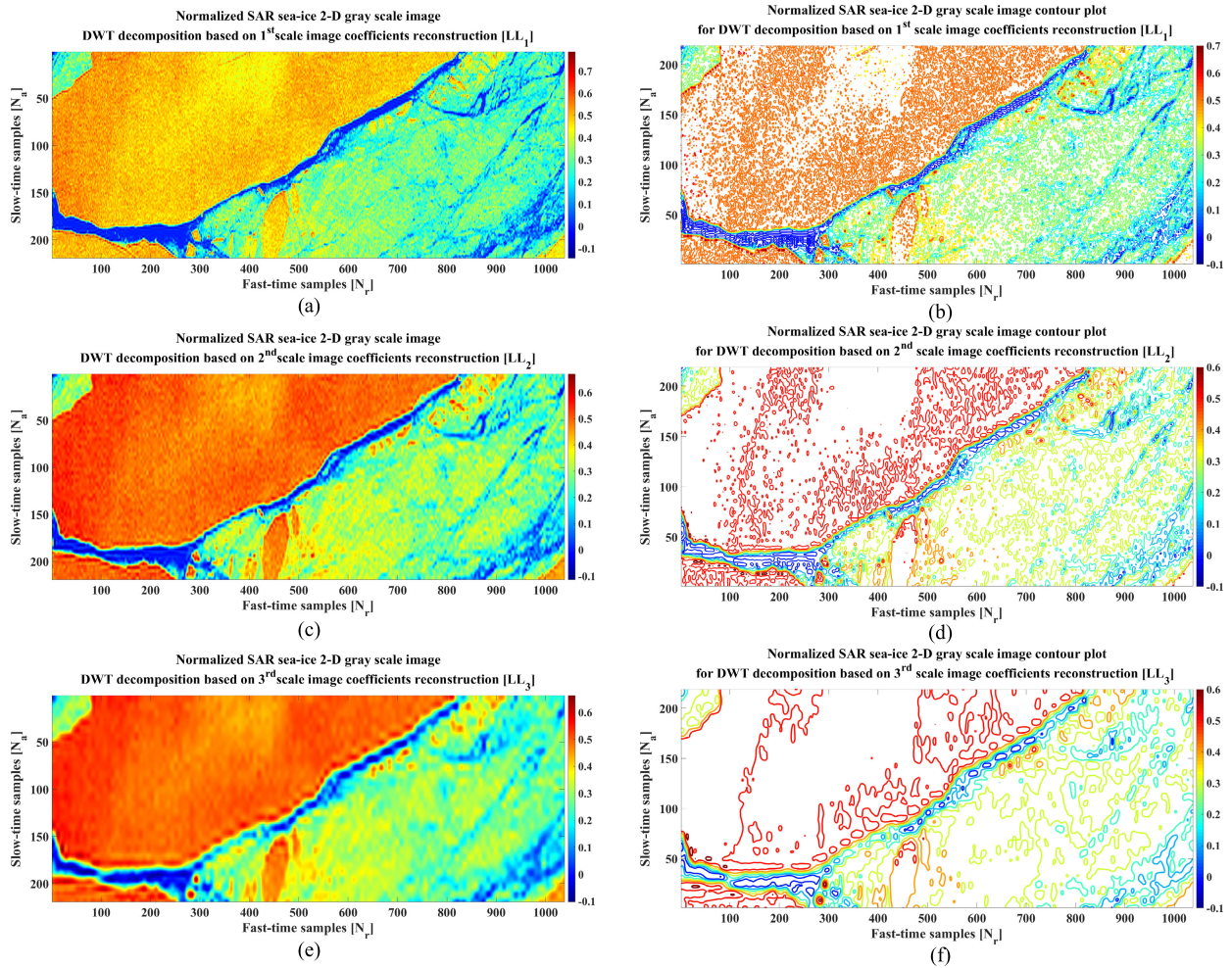


FIGURE 16. Normalized SAR sea-ice DWT-decomposed images: (a) 1st scale, (b) 1st-scale contour plot, (c) 2nd scale, (d) 2nd-scale contour plot, (e) 3rd scale, and (f) 3rd-scale contour plot.

of known number of clusters and centroid initialization. The next section will present the segmentation results in detail.

III. SIMULATION RESULTS AND VERIFICATION

For highly deformed textures and with low cross-correlation terrains, such as SAR sea-ice images, there may be useful texture information affected by HMN, and its suppression is crucial to postprocessing. Hence, a comprehensive fractal analysis of HMN and its effects on the texture classification could be considered helpful. Accordingly, the reference KOMPSAT-5 SAR sea-ice image in Fig. 1 will be investigated based on DWT decomposition and properties extraction as well as the classification. The total objective quality assessment carried out at each step of investigation helps us understand the adverse effects of HMN presence. To the best of our knowledge, this is the first time that a KOMPSAT-5 SAR sea-ice image is being decomposed, modeled, classified and verified on the basis of TFD multiplicative noise suppression. The objective quality assessment uses both qualitative and quantitative metrics that verify procedure. The metrics are the

image resolution, spatial resolution, pixel-based, correlation-based, SAR parameters, spectral properties and tensor field mapping.

A. KOMPSAT-5 SAR SEA-ICE TEXTURE DECOMPOSITION AND HMN SUPPRESSION BASED ON THE DWT METHOD

The DWT multiresolution method transforms sea-ice images into representations in which both spatial and frequency information are presented with multiple scales along the fast-time and slow-time directions. The reconstructed images are the standard pyramidal decompositions with the same number of pixels as that in the reference image (Fig. 14). Among the images, the one that is obtained by vertical and horizontal low-pass filtering, contains the maximum information of the sea ice (LL). LL_1 is selected for the next round of multiscale decomposition in the same manner as that for the reference image. From the next round of decomposition, the approximated LL_2 is extracted. Similarly, the decomposition will continue to further scales since at the third scale, the image loses some of its anomaly details as LL_3 .

According to Fig. 14 and the proposed SAR sea-ice image in Fig. 1, the results of DWT decomposition as well as the texture contour plots are presented in Fig. 18. As shown, the texture including the ice floes, ice fragments, sea-ice and open waters are still distinguishable based on their values, although they are visually getting smoother as the decomposition continues at further scales. The contour plots verify the presence of pixel anomalies and backscattered coefficient alteration suppression between adjacent spatial resolution cells according to their magnitude and concentration. Accordingly, as a result of HMN suppression and texture smoothing, the image resolution profile in both the fast-time and slow-time directions is extracted and shown in Fig. 17.

It can be deduced that pixel intensity alterations, including abrupt changes and slow variations in both the fast-time and slow-time directions, are not only damped at every scale of DWT decomposition but also the intensities of the remaining pixels are amplified as the decomposition continues. Figures 17(c) and 17(d) show a value of maximum 0.6 dB pixel amplification at each scale of the decomposition compared to the previous scale, while the total amplification for three scales of decomposition is approximately 2.6 dB.

Similarly, the deteriorative effects of HMN on the image frequency profile while being decomposed have been extracted and are shown in Fig. 18. Based on the results, the HMN level has been suppressed by approximately 3 dB in both the fast-time and slow-time directions as the spectrum becomes sharper in the peak and flattened in the side lobes while being decomposed into further scales. This frequency profile modification directly affects the instantaneous pixel alterations and anomaly correction, which are the results of the presence of uncorrelated HMN and its spectral tailedness.

Accordingly, the rate and intensity of pixel anomalies will be damped and corrected, as shown in Fig. 19. The total correction value reaches approximately 0.8 dB, and it is clear that the third scale of decomposition is completely successful in pixel anomaly correction. It should be noted that HMN suppression and tailedness flattening directly affect the GVF. As shown in Fig. 20, the vectors are becoming highly focused while the field concentrations on the boundaries are higher due to pixel anomaly correction as the decomposition continues. In other words, HMN is the reason for the nonuniform vector field distribution throughout the entire sea-ice terrain, and it degrades the image quality by way of pixel intensity anomalies. These phenomena have adverse effects on the image resolution and vector field dissipation on the basis of the probability distribution by way of different gradient values and angles of probability, which are completely responsive to the GVF corrections.

The results in Figs. 21 and 22 verify that the SAR sea-ice areas with anomalies are sensitive to gradient value changes, which are previously introduced as unstable areas. In short, the unstable areas with larger gradient values and angles of probability are most likely to be the source of HMN, specifically those places that are boundaries and contain thin ice and open water at the same time.

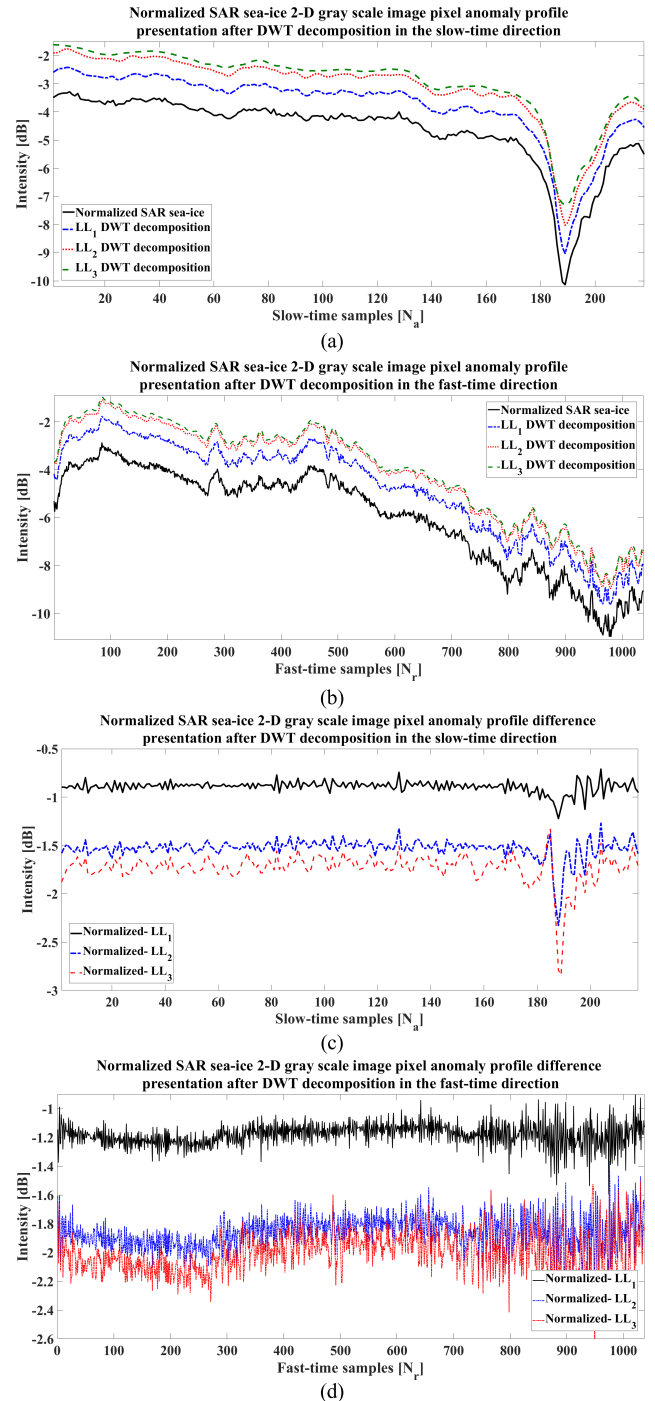


FIGURE 17. Normalized SAR sea-ice DWT-decomposed image pixel anomaly profile presentation and comparison (a) slow-time (b) fast-time (c) slow-time difference profile (d) fast-time difference profile.

The DWT decomposition is completely helpful for HMN suppression as well as resolution enhancement. It is clear from the results that the flat or peaky HMN distribution decreases at each scale of the decomposition specifically in unstable regions. The abovementioned results are also true for the SAR spatial resolution effects analysis. According to Figs. 1, the nonhomogeneous sea-ice structure does not

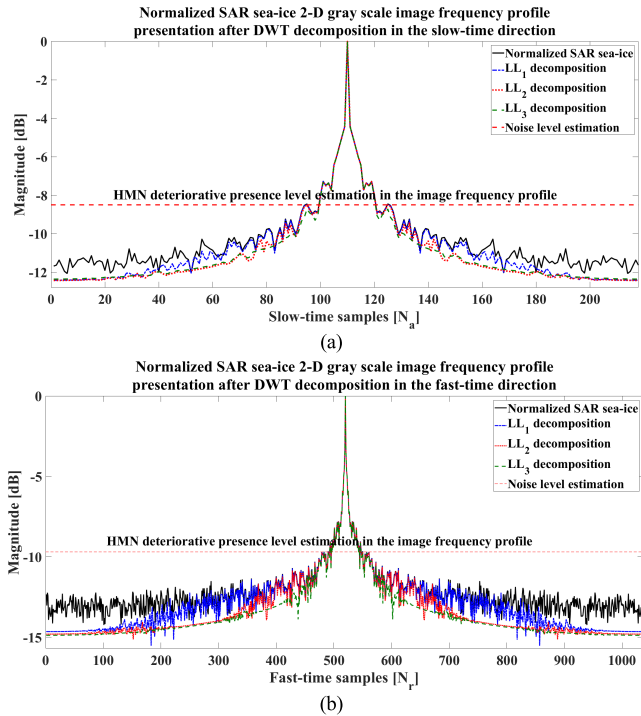


FIGURE 18. Normalized SAR sea-ice DWT-decomposed image frequency profile presentation (a) slow-time and (b) fast-time.

follow a specific pattern when dealing with electromagnetic pulses. In other words, the structure of sea-ice has partially direct adverse effects on the coherency of the electromagnetic interactions and imposes a random walk of magnitudes and phases in the superposition of reflections. The result is random radiometric fluctuations associated with any resolution cells that are identically distributed in the real and imaginary part of the received backscattered data. This pattern of embedded uncorrelated and noncoherent noise is formed when each resolution cell contains many point scatterers pertaining to resolution cells that are much larger than the wavelength of the incident wave that presents in a Rayleigh distribution of the intensity fluctuations within a sea-ice image, while none of which produces a significant reflection by itself. Accordingly, the presence of HMN over the 2-D received backscattered sea-ice data and the intensity fluctuation advection maps are shown in Fig. 23. The results verify the random pattern of the presence of HMN based on the probability function and intensity distributions. According to Figs. 23(c) and 23(d), DWT decomposition reduces the intensity fluctuation in the entire sea-ice scene. The overlaid result of the sea-ice HMN kurtosis and the reference image in Fig. 23(e) shows how the sea-ice structure forms the pattern of HMN over the entire terrain.

The results in Fig. 24 show that this uncorrelated and noncoherent pattern known as HMN has an attenuation of at least 1 dB on the received backscattered signal magnitude that could easily affect the information capacity for each resolution cell while being received by the receiver.

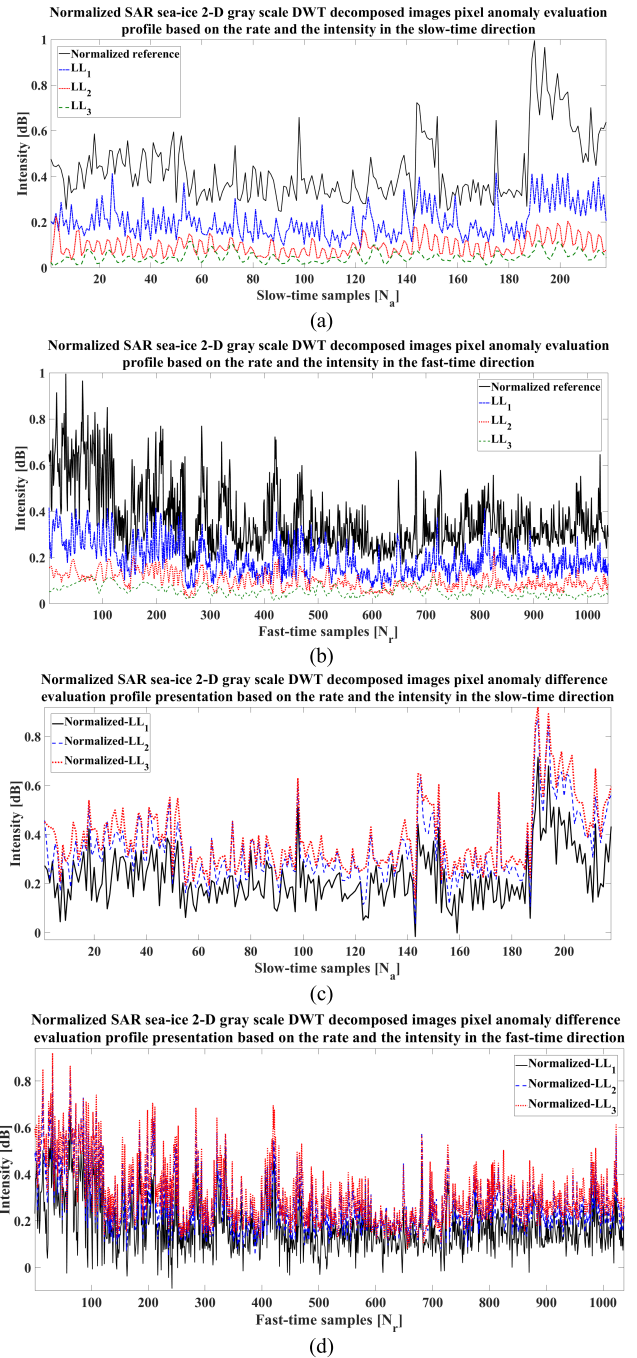


FIGURE 19. Normalized SAR sea-ice DWT-decomposed image pixel anomaly evaluation based on the rate and intensity: (a) slow-time direction, (b) fast-time direction, (c) slow-time difference direction profile, and (d) fast-time difference direction profile.

Accordingly, it can be deduced that the decomposed images are very similar to the reference image in terms of the pixel-based metrics, and HMN suppression has not changed the pixel intensity distributions; the results are listed in Table 2.

The source of the pixel anomalies and their distribution are shown in Fig. 25(d). It is clear that sea ice, which includes open water and thin ice sheets, is the major source of HMN

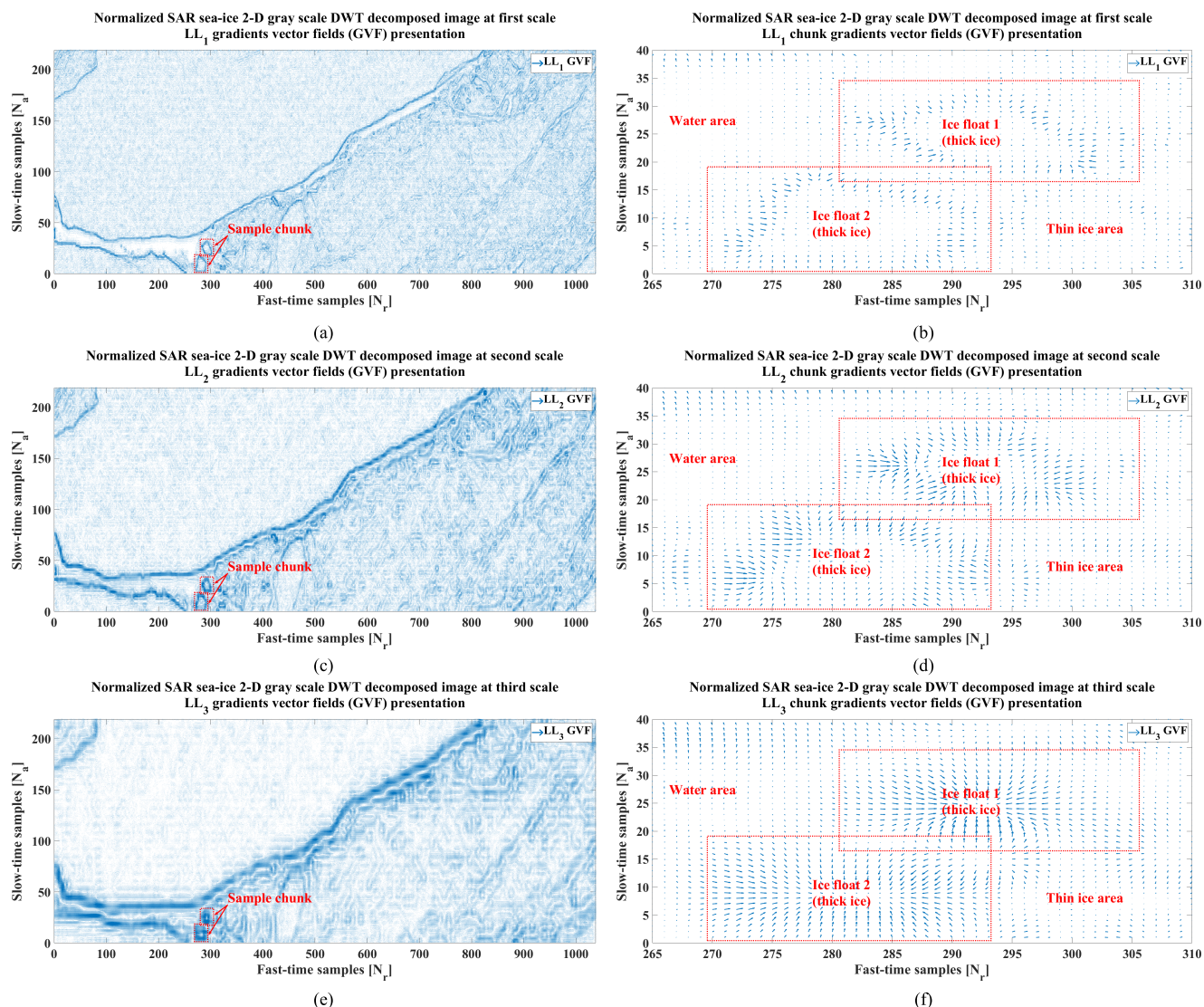


FIGURE 20. Normalized SAR sea-ice DWT-decomposed image gradient vector field presentation: (a) 1st scale, real size; (b) 1st scale, zoomed-in view; (c) 2nd scale, real size; (d) 2nd scale, zoomed-in view; (e) 3rd scale, real size; and (f) 3rd scale, zoomed-in view.

TABLE 2. Decomposed SAR images’ pixel-based objective quality metric results.

Image	MSE	MIV	Var.	SNR [dB]	PSNR [dB]	SSIM	MSSIM
Reference	-	0.36	0.02	16.11	-	-	-
1st scale	0	0.36	0.02	15.99	26.07	1	0.99
2nd scale	0	0.36	0.02	14.82	24.00	1	0.99
3rd scale	0.01	0.36	0.01	14.89	22.73	0.97	0.95

and consequently the pixel anomalies, while its PSNR is approximately 7.5 dB and the variance and mean intensity value (MIV) are zero.

The same results are derived while correlation-based measurements are being calculated. According to Fig. 26, all the DWT-decomposed images, including the first scale and the second and third scales, have the highest degree of similarity

to the reference image based on a normalized cross correlation (NCC) value of 8.7 in both the fast-time and slow-time directions. Similarly, Table 3 and Fig. 27 show the evaluation results of the quantitative metrics for the DWT-decomposed SAR images. As can be deduced, HMN suppression can improve the received signal strength in the receiver but reduce the PSLR and ISLR values at the same time. It should be noted that despite SAR-specific metric degradation based on decomposition, spatial information is retained within the signals, and all the indexes still have acceptable values and are far from undesired thresholds.

B. KOMPSAT-5 SAR SEA-ICE TEXTURE AND EMBEDDED HMN SPECTRAL MODELING BASED ON THE JOINT COMPLEX TFD METHOD

From the SAR spectral point of view, a SAR grayscale image of a time-dependent terrain can be regarded as an independent mapping of an ensemble of various scatterers having

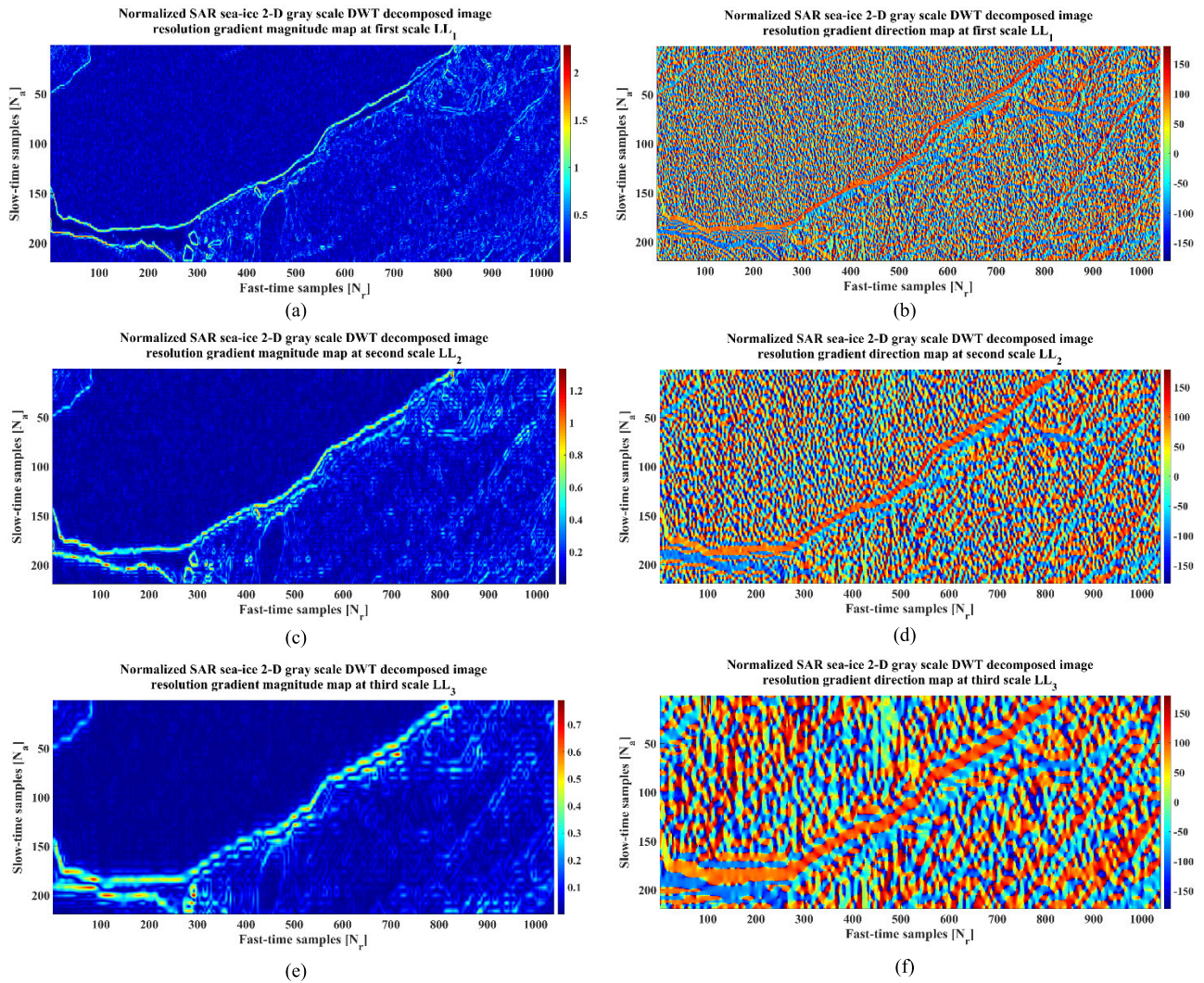


FIGURE 21. Normalized SAR sea-ice DWT-decomposed image resolution gradient and direction maps: (a) 1st scale, (b) 1st scale, (c) 2nd scale, (d) 2nd scale, (e) 3rd scale, and (f) 3rd scale.

TABLE 3. SAR sea-ice metric evaluation results.

Image	PSLR [dB]	ISLR [dB]
Reference	-27.6	-12.7
1st scale LL ₁	-25.5	-13.7
2nd scale LL ₂	-18.1	-12.06
3rd scale LL ₃	-15.6	-6.9

different Doppler frequencies into different, azimuthally displaced imaging points. These phase points are synchronized, frame formatted and reassembled based on the observation mode and the illumination time. On the other hand, the DWT of the reconstructed image will conveniently decompose the aforementioned data on the basis of a specific scale and orientation while retaining their spatial information. As a result, statistical pixel distribution analysis based on the amplitude, phase, and intensity will enhance texture decomposition and sensor-terrain interaction investigations. This statistical moment investigation with the help of the underlying spatial

distribution will result in PSD function extraction, which is considered a combined spectral analysis of the entire terrain [4]. The PSD function can model the intensity of the joint pixels as a function of a certain interval of frequencies and provides information on the energy associated with a specific range of frequencies. According to Figs. 10 and 16, the modeled PSD function of the normalized reference KOMPSAT-5 sea-ice image and its received backscattered data are presented in Fig. 28.

Figure 30 also includes the difference in the PSDs between the reference SAR sea-ice image and the reconstructed DWT-decomposed images. The major low-frequency peak in the PSD function in Figs. 28(a) and 28(c) represent the spatial statistics of the main body of the sea-ice structure and the received backscattered data. Both the reference image and the received backscattered data consist of a single peak in the low-frequency part of the PSD function, which is a sign of a nonoverlapping structures in the sea-ice texture known as a major entity. The received backscattered data and the

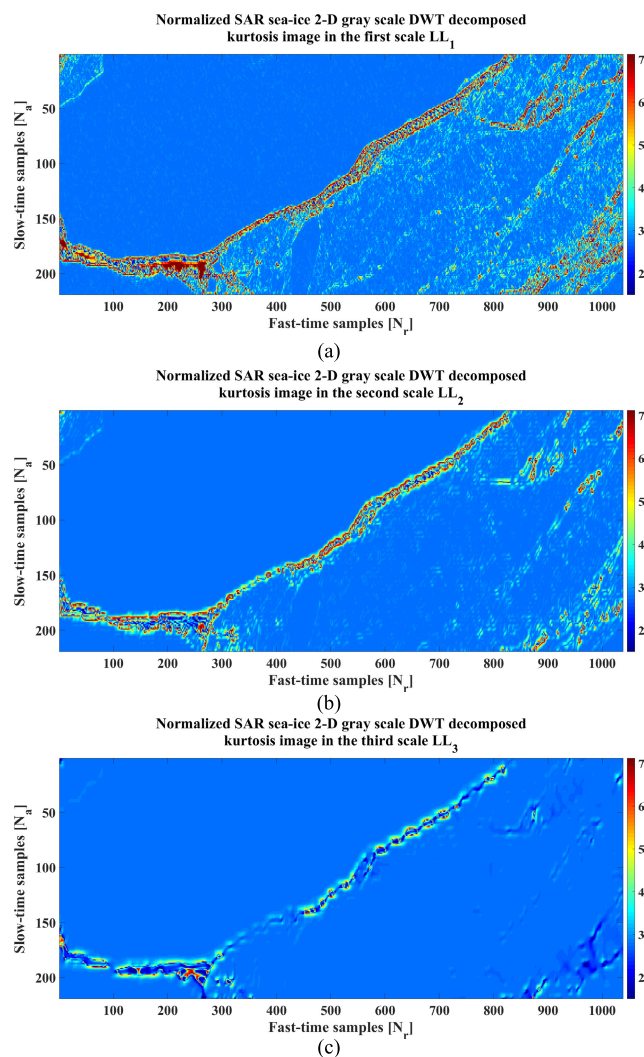


FIGURE 22. Normalized SAR sea-ice DWT-decomposed image kurtosis: (a) 1st scale, (b) 2nd scale, and (c) 3rd scale.

reference image have an approximately 12 dB difference in the PSD intensity profile, which is due to the probable loss effects, which can be measured by the received signal strength (RSS). According to the result in Fig. 28(b), all the decomposition images have almost the same spectral distribution with a magnitude of approximately 13 dB in the low-frequency part of the PSD function, while the maximum PSD difference value belongs to the third scale DWT-decomposed LL_3 with a difference of 0.12 dB. The other previous decomposition scales, such as LL_1 and LL_2 , mostly behave the same as the reference image, which shows that their resulting textures based on the pixel distribution and estimation are the same. Similarly, PSD function modeling is carried out for the purpose of sensor-terrain embedded noise interaction. As seen in Figs. 28(d), the PSD of the sea-ice backscattered data is mostly contaminated with embedded HMN with a magnitude of 0.012 dB that is located in the entire high-frequency and partially the medium-frequency parts of the raw data, which is completely dependent on the backscattering conditions.

Similar to Fig. 28, PSD function modeling is carried out for the purpose of pixel anomaly distribution over the entire SAR sea-ice texture while being decomposed based on DWT, which is shown in Fig. 29. The same as in Fig. 29(d), the embedded noise has occupied the entire high-frequency part of the PSD due to their spatial locations in terms of the adverse overlapping multiplicative distribution, which has significant adverse effects on the amplitude, phase and intensity.

Compared to the major entity of the texture, the pixel anomalies can be modeled as high-frequency replication structures within the PSD function in the shape of several high-frequency peaks. As presented in Fig. 29, the PSD of the HMN distribution in LL_2 shifts to the medium-frequency parts, while in LL_3 , the HMN distribution approaches the low- and medium-frequency parts of the function, which is the same as the major peak in Fig. 28. As the decomposition continues, not only is the HMN distribution reduced but their presence levels and spatial frequency locations are also altering. In other words, higher orders of DWT decomposition consist of major nonoverlapping structures with significant variance that are not reduced to the replication of anomaly statistics.

In short, further scales of the DWT decomposition are no longer effective because the HMN spatial distribution has completely shifted toward the low-frequency parts of the PSD, which shows that the HMN behaves the same as the main entity of the texture but with different statistics and distribution variances. According to Figs. 29(a) and 29(b), the intensities are, to some extent, on the same margin, but in Fig. 29(c), not only the HMN spatial locations shifted toward the low-frequency parts but its magnitude also increased five times.

As a result, the pixel anomaly removal or HMN suppression at higher scales of DWT decomposition are more likely to be the same as the suppression of main-body information and not the HMN per se. It should be noted that the HMN distribution function is supposed to be a general gamma distribution. As shown in Fig. 16, the DWT decomposition makes the images visually smoother, and it is necessary to compare the decomposition effects based on the structural visualization of the texture while considering the pixel distributions. To validate the pixel anomaly correction with the help of DWT decomposition, tensor field map (TFM) visualizations can provide proper information about the structural properties of HMN suppression within the texture on the basis of spatial configurations. Accordingly, the elliptic visualizations for a group of pixels with specific colors ranging from blue to red are shown in Fig. 30. Blue indicates the presence of normal anomalies, and red indicates a high rate, while their axes can be oriented toward specific directions in the shape of an ellipse. This presentation is based on the magnitude, direction and ratio between the samples that can detect possible anomalies with different local behaviors than the surroundings. In the case of homogenous areas such as thick ice floes that spatially handle the uniform change in

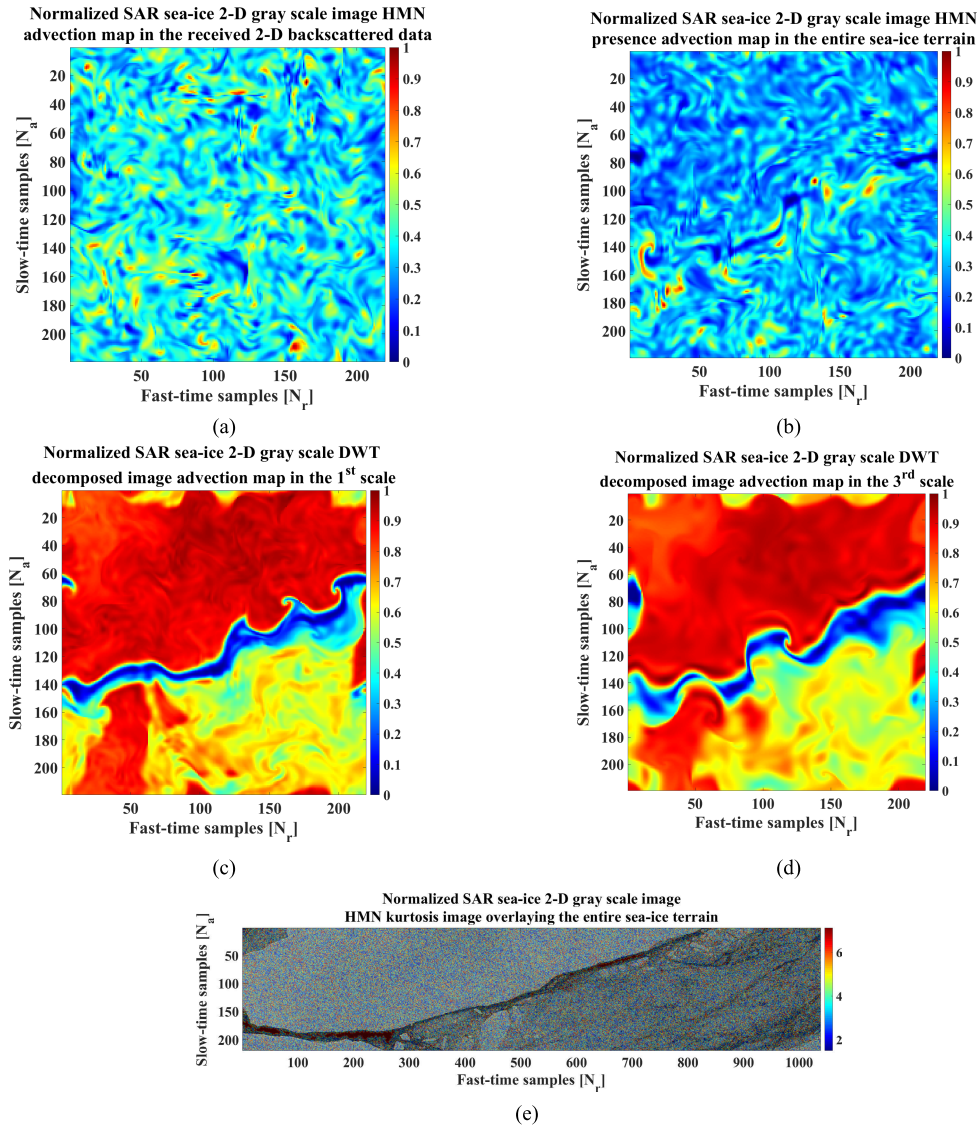


FIGURE 23. Normalized SAR sea-ice HMN (a) advection map of the 2-D received backscattered data, (b) advection map of the sea-ice terrain, (c) advection map of the 1st scale of DWT decomposition, (d) advection map of the 3rd scale of decomposition, and (e) the results overlaid on the reference image.

pixel statistics, the direction and the axis size of the ellipse are almost similar to a circle.

However, as the intensity of changes increases sharply in each principal direction that is the same as that of ice drifts or open water, not only the shape of elliptical descriptors will change based on their tensor eigenvector and eigenvalue calculations but also their orientation is changing at the same time with different colors. In other words, blue indicates a normal anomaly, and red indicates a high rate, while the axes are aligned on the basis of magnitude, direction and the ratio between the samples that can detect possible anomalies with different local behaviors than the surroundings. The results in Fig. 30 completely present the TFM visualization alteration within the reference SAR sea-ice image as the decomposition continues.

It is clear that the third scale of DWT decomposition, LL₃, could be the last scale for anomaly correction, while there have just been oriented lines instead of circles or ellipses that show how much intensity change is in each principal direction. The results in Fig. 30 are completely in agreement with the results in Fig. 23, which shows HMN suppression and pixel anomaly corrections.

C. KOMPSAT-5 SAR SEA-ICE TEXTURE CLASSIFICATION RESULTS BASED ON THE K-MEANS CLUSTERING METHOD

As described in Section II.B.3, the K-means clustering algorithm tries to partition the SAR sea-ice image into pre-defined, distinct, nonoverlapping clusters where each pixel

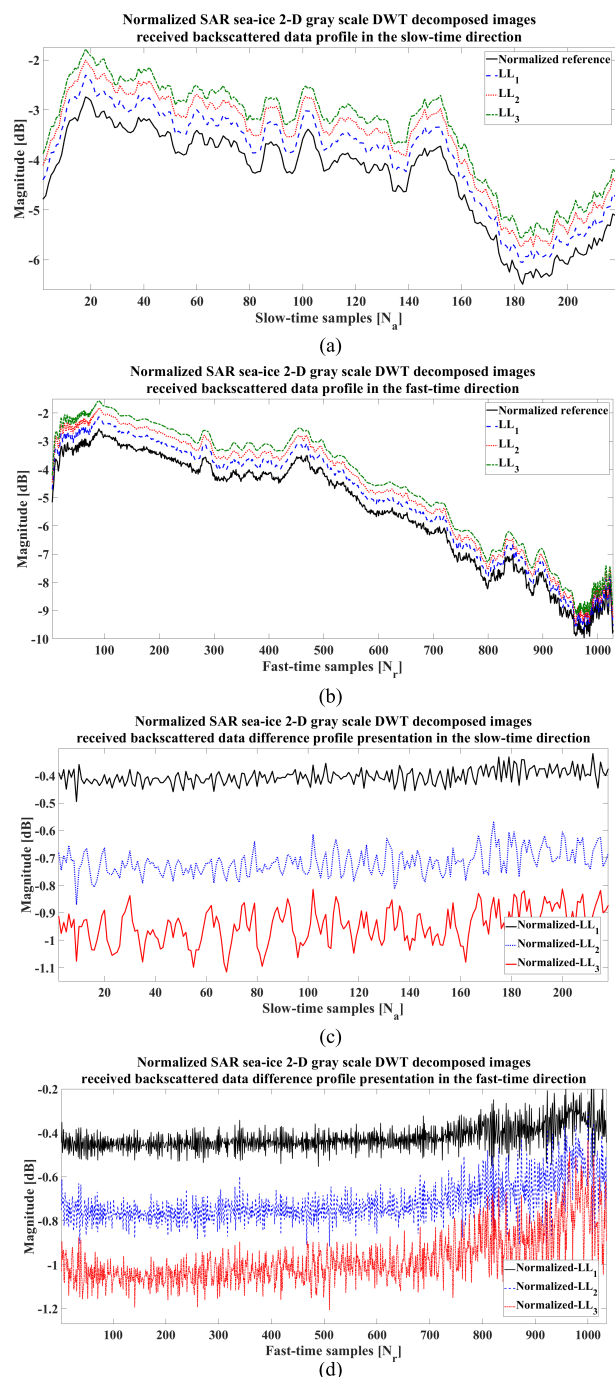


FIGURE 24. Normalized SAR sea-ice DWT-decomposed image spatial resolution profile presentation and comparison (a) slow-time (b) fast-time (c) slow-time difference profile (d) fast-time difference profile.

belongs to only one group, while the difference between the pixels and the cluster’s centroid index is minimized. The clustering tries to make the intercluster pixels as similar as possible while also keeping the clusters as different as possible. The less variation we have within clusters, the more homogeneous the segment is. The prior information about the reference SAR sea-ice image, the pixel anomaly behavior, the image DWT decomposition and the fractal analysis

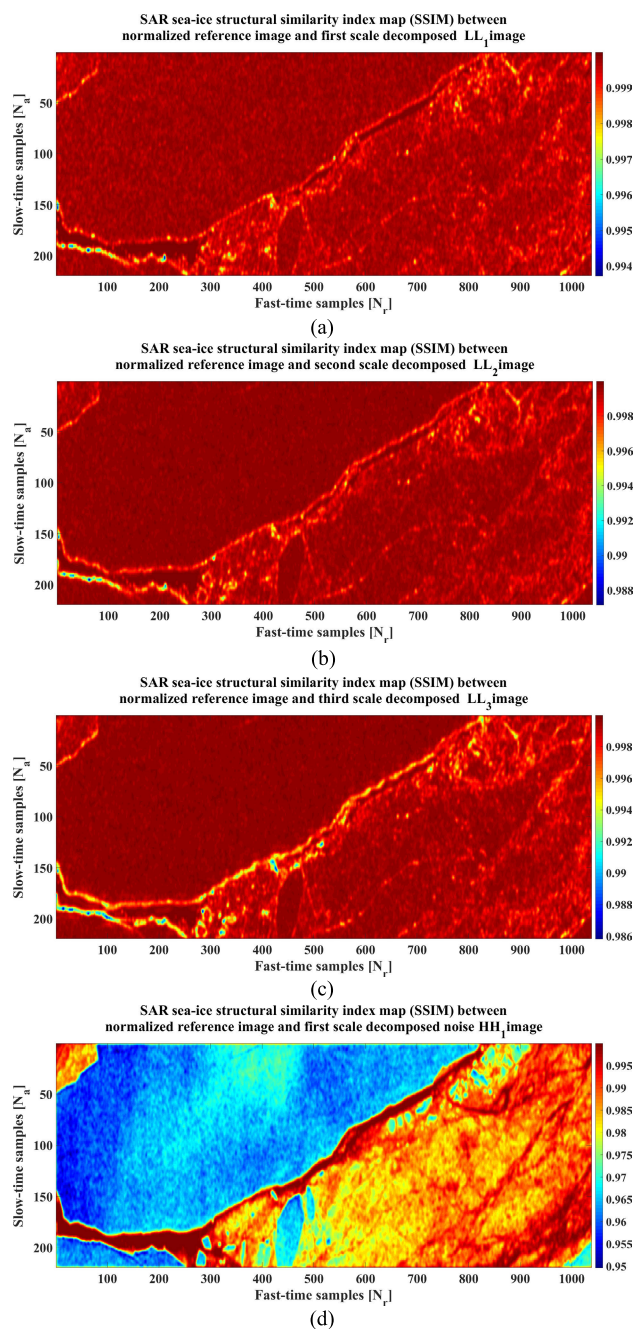


FIGURE 25. Normalized SAR sea-ice DWT-decomposed image SSIM map: (a) 1st scale, (b) 2nd scale, (c) 3rd scale, and (d) the 1st scale diagonal HH₁.

that have been described in the previous sections will affect the results of unsupervised classification evaluation of this section. For the sake of validity, unsupervised K-means clustering is carried out based on two different algorithms (iterative and adaptive) on the reference SAR sea-ice image and its DWT-decomposed versions under the same simulation conditions. It should be noted that in the iterative clustering algorithm, the numbers of clusters are predefined as five and four clusters.

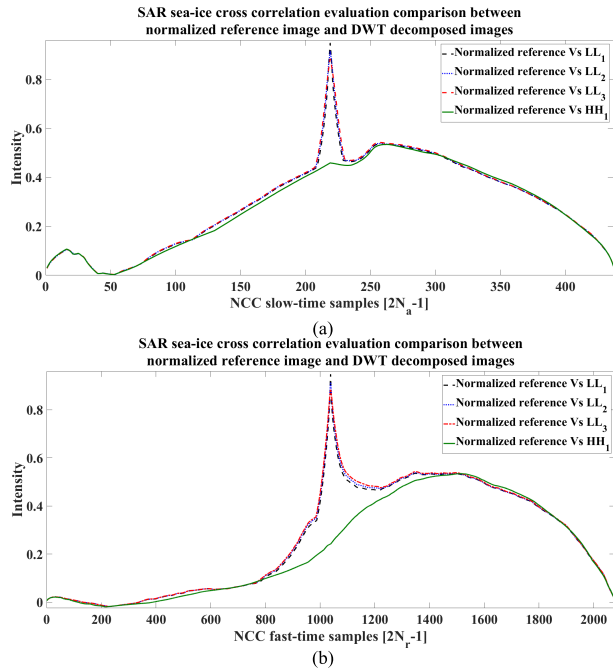


FIGURE 26. Differences in the NCCs between the reference normalized SAR image and the DWT-decomposed image; (a) slow-time and (b) fast-time.

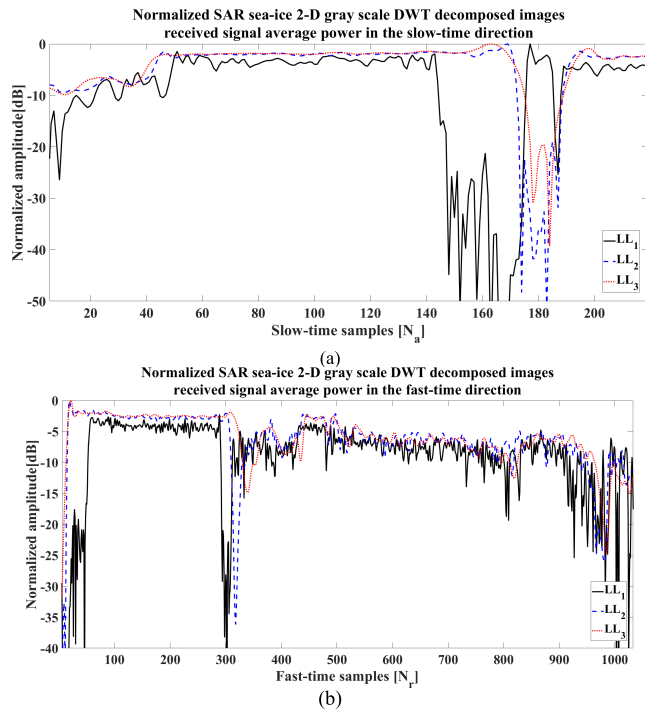


FIGURE 27. Normalized SAR image DWT-decomposed image average received signal intensity; (a) slow-time (b) fast-time.

However, the adaptive clustering number derivation is completely based on the convergence of the results. Accordingly, the results of both the iterative and adaptive versions of the unsupervised K-means classification algorithm are

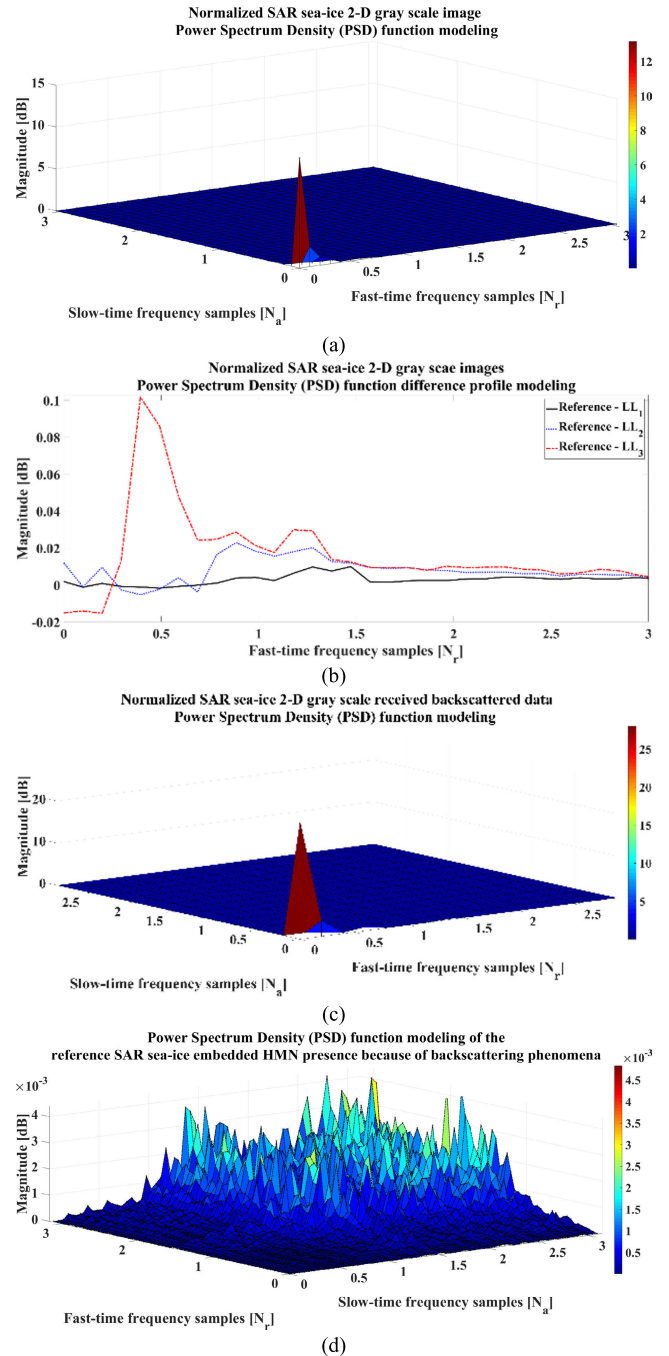


FIGURE 28. Normalized SAR sea-ice image PSD function modeling of (a) the reference image, (b) the DWT-decomposed image difference profile, (c) the received backscattered data, and (d) the received backscattered data HMN.

presented in Figs. 31 and 32. According to the results and on the basis of the number of clusters and the classification results, it is deduced that sea-ice segmentation on the basis of DWT decomposition has better results rather than the reference version.

As seen, the differentiation between textures improves as the decomposition continues. As a rule of thumb, the higher the DWT decomposition scale is, the better the

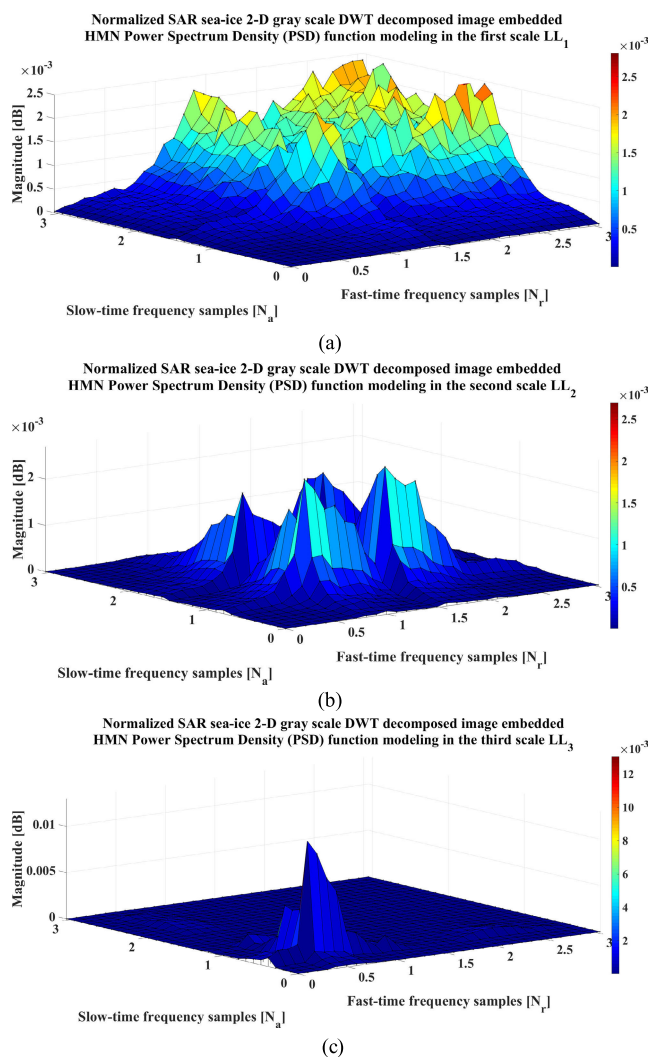


FIGURE 29. Normalized SAR sea-ice DWT-decomposed image PSD function modeling at the (a) 1st scale, (b) 2nd scale, and (c) 3rd scale.

segmentation results are. However, the proper selection of the DWT scale remains a challenge based on the details in Sections II.A and III.B. According to the iterative K-means simulation results in Figs. 31(a) and 31(b), by the time the clustering is addressing the reference normalized SAR sea-ice image, the iterative clustering results are supposed to be nonuniformly grouped in comparison to the adaptive clustering result in Fig. 32(a). This finding shows that the iterative clustering is completely sensitive to the adverse effects of HMN and the presence of pixel anomalies within the texture, while the adaptive version works better under the same conditions. On the other hand, the other adaptive clustering results in Fig. 32 demonstrate that in adaptive clustering, there is a specific difference in the clustering between the real reference SAR image and its DWT-decomposed images.

In other words, the adaptive K-means clustering algorithm is superior to the iterative version while being applied on the reference SAR image. However, the superiority of adaptive clustering when ignoring the presence of HMN and its

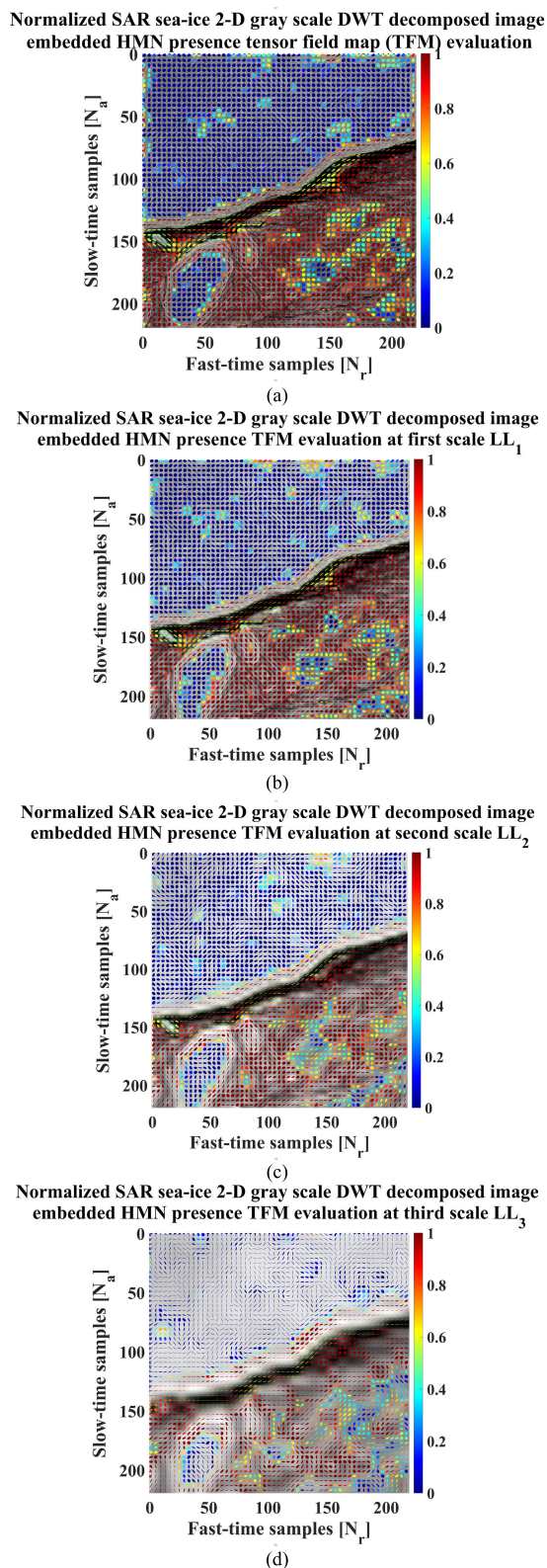


FIGURE 30. Normalized SAR sea-ice DWT-decomposed images, TFM visualization presentation: (a) the reference image, (b) the 1st scale, (c) the 2nd scale, and (d) the 3rd scale.

adverse effects on the pixel anomalies in the reference SAR image could also be considered a defect in high-resolution SAR images at the same time even if it functions with an

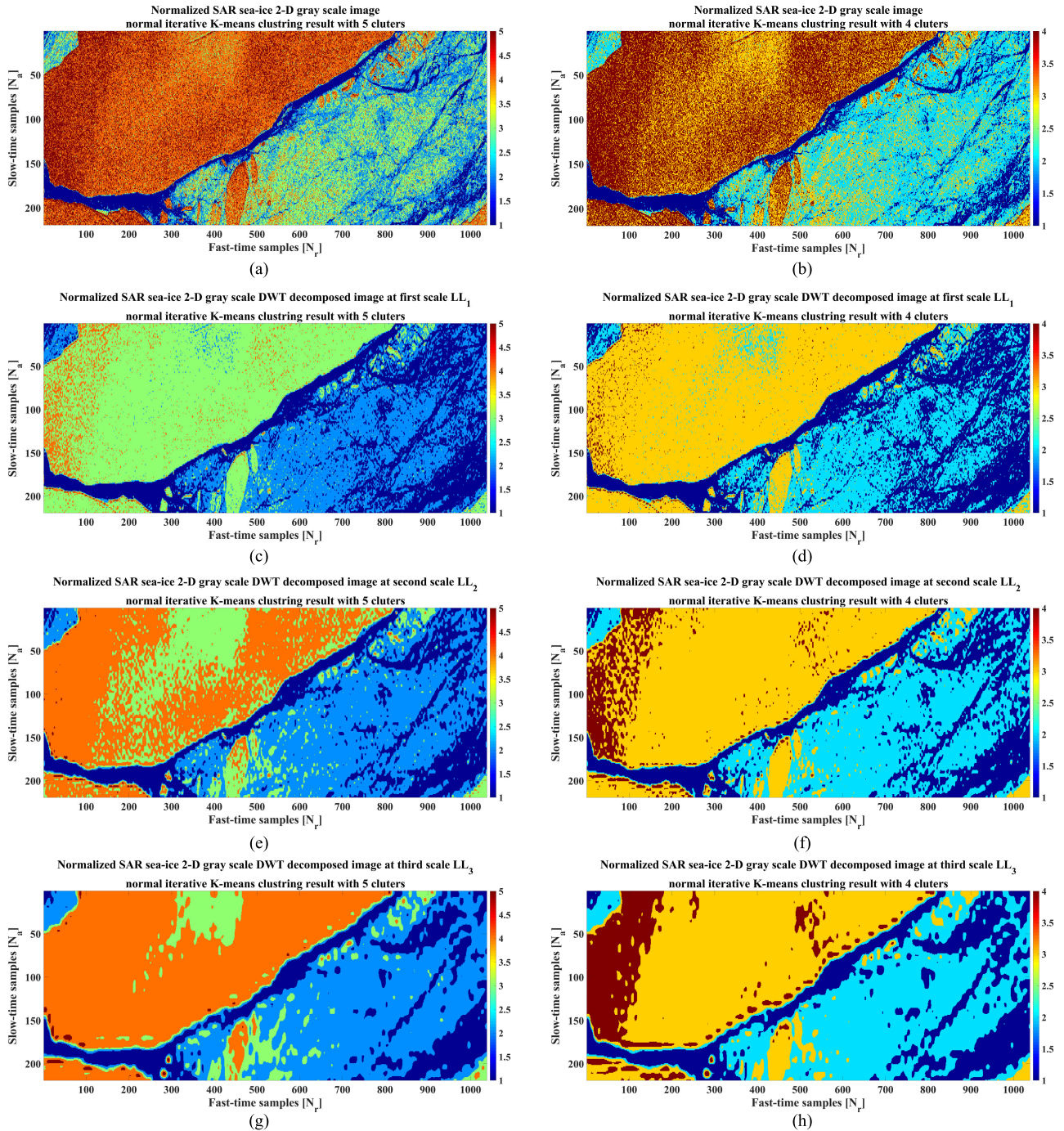


FIGURE 31. Normalized SAR sea-ice image iterative K-means clustering results: (a) the reference, (b) the reference, (c) the 1st scale, (d) the 1st scale, (e) the 2nd scale, (f) the 2nd scale, (g) the 3rd scale, and (h) the 3rd scale.

automatic number of clusters. Accordingly, as both clustering methods are being applied directly to the DWT-decomposed images, the precision of grouping the pixels into specific clusters increases, specifically in the homogenous sea-ice textures, such as ice floes, borders, areas surrounding ice fragments and open water.

It is deduced from the results that at higher scales of DWT decomposition and simultaneously with HMN suppression,

clustering works better than at the lower scales. In general, the most desired K-means clustering results could be considered as those in Figs. 31(e) to 31(h) or Figs. 32(c) and 32(d). Nevertheless, in the case of clustering evaluation and verification, not only should pixel anomaly suppression be considered but also the acceptable similarity between the clustered images must be taken into account. In other words, according to the iterative clustering results in Figs. 31(a) and 31(b),

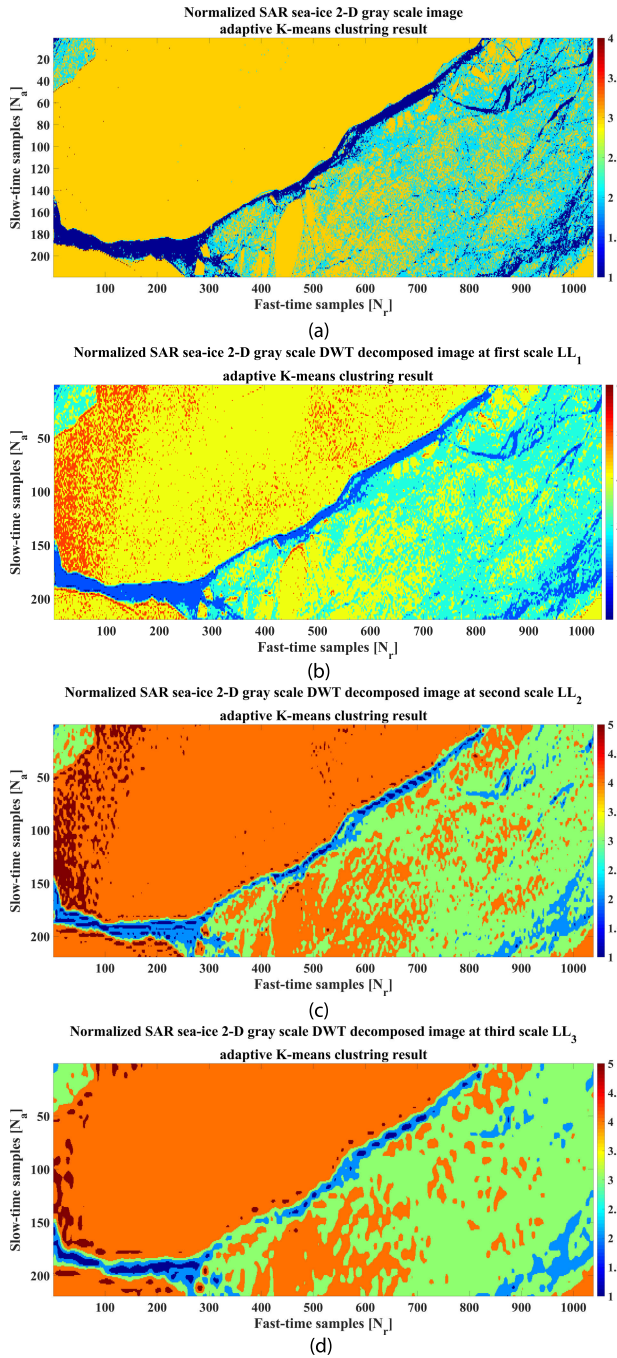


FIGURE 32. Normalized SAR sea-ice image adaptive K-means clustering results: (a) the reference, (b) the 1st scale, (c) the 2nd scale, and (d) the 3rd scale.

we propose first suppressing the adverse effects of HMN with the help of DWT decomposition. The selection of the proper scale for DWT decomposition could be done with the help of the results in Section III. A and B and the number of convergence adaptive clusters. In the case of SAR sea-ice and according to the results in Figs. 29, 31 and 32, the best scale of DWT decomposition is considered the second scale. In the second scale, not only has the HMN been suppressed

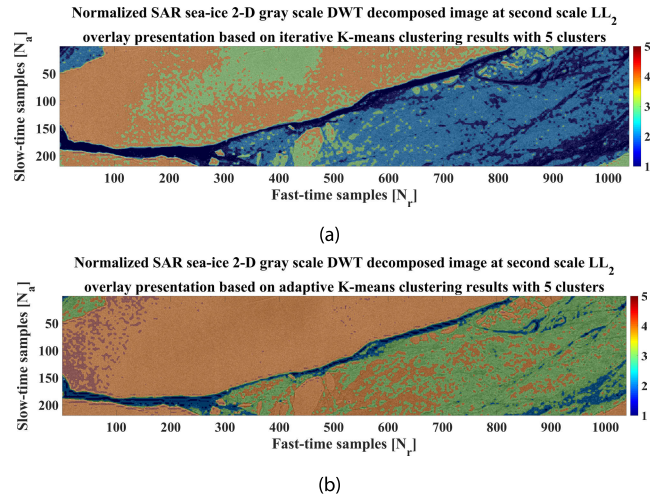


FIGURE 33. Normalized SAR sea-ice third DWT decomposition clustering results comparison: (a) iterative K-means and (b) adaptive K-means.

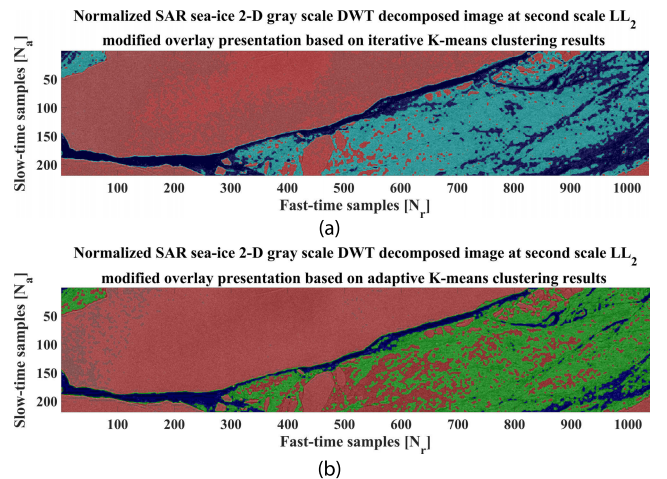


FIGURE 34. Normalized SAR sea-ice third DWT decomposition modified clustering results comparison: (a) iterative K-means (b) adaptive K-means.

properly but both the adaptive and the iterative clustering algorithms have converged in their segmentation number, and their clustered maps are almost similar.

In short, DWT-decomposed images have better clustering results than the reference image, while the adverse effects of pixel anomalies on the clustering results are shown in Figs. 33(a) and 34(a). It is also deduced that the adaptive K-means clustering algorithm is the same as the iterative version and does not have the ability to classify the structures with highly complicated electromagnetic interactions such as edges, while HMN suppression makes it possible. In other words, better classification results against the presence of HMN means that the false alarms have been successfully suppressed in the reference image. Figs. 33 and 34 present and overlay images of the clustered DWT results and the reference SAR image for a better visualization, while their modified clustering versions are also presented.

The ultimate goal of this section is to classify the sea-ice texture in SAR images to facilitate the subsequent analysis. The results of DWT decomposition have been used to generate clustered images while the HMN has been suppressed and analyzed. According to the whole the K-means clustering procedure, not only has the HMN been suppressed properly but also the clustering is close to the most likely unsupervised condition, which has been derived based on two different algorithms. As a result, the presence of pixel anomalies due to the adverse effects of HMN will result in segmentation errors, and the selection of the proper scale of DWT decomposition on the basis of a quality assessment technique is the key for SAR sea-ice texture analysis. According to the results above, it is important to suppress the HMN while it belongs to the high-frequency part of the data, and PSD modeling plays an important role in proper scale selection for decomposition.

IV. CONCLUSION

The KOMPSAT-5 SAR sea-ice image resolution is inherently degraded by phase interferences of received backscattered signals in the form of pixel anomalies known as noncoherent HMN. According to the fractal sea-ice resolution profile, HMN is dependent on the underlying radar reflectivity characteristics and presents itself as a nonspecific pattern of pixel anomalies. It is also shown that due to the multilayer structure of sea-ice, the notion of the texture is associated with HMN and might reflect erroneous information on the inherent properties of the texture, which leads to misinterpretations. Thus, it is necessary to assess the adverse effects of the presence of HMN on KOMPSAT-5 SAR sea-ice texture while developing a suppression technique for anomaly correction.

Accordingly, a TFD suppression technique based on DWT decomposition is proposed in this research. Since the DWT algorithm is sensitive to intensity variations at the given scale of decomposition and HMN has scale-dependent properties, a distribution model of the HMN at each scale of decomposition has been provided. According to the asymmetrical PDF formulation and multiresolution spectral behavior modeling at the decomposition scales, the nonlinear behavior of HMN that can modulate the DWT coefficients and lead to texture irregularities as the source of information loss has been simulated and presented. It is also shown that the noncoherent HMN will change the DWT coefficients proportionally to the mean reflectivity of the terrain. Thus, it is important to assess the adverse effects of HMN on DWT decomposition before it is used for texture classification.

The proposed novel approach is tested on real KOMPSAT-5 SAR sea-ice images as well as on simulated images to quantify the percentage of correct classifications. Several fractal indexes proposed in this research are completely new and are considered for SAR sea-ice image texture analysis for the first time. The most important metrics including PDF formulation and PSD analysis of the HMN at each scale of decomposition, raw data generation for the DWT-decomposed images, sea-ice resolution fractal analysis, tensor field map presentation of the adverse effects of HMN, HMN pixel anomaly

advection mapping, pixel anomaly edge gradient vector mapping and several objective quality assessment metrics. For the purpose of further verification, two different types of K-means clustering algorithms were used and compared, which shows the reliability of the approach. Finally, it should be noted that a fully developed HMN pattern is the magnitude of the complex reflectivity coefficient distribution function with a correlation structure dependent on the waveform shape, sensor electromagnetic interactions, imaging mechanism and the geometry involved. Notably, the entity of the terrain being imaged plays a key role.

ACKNOWLEDGMENT

The authors would like to thank the Korea Polar Research Institute (KOPRI) for providing all facilities for this research.

REFERENCES

- [1] C. F. Barnes, *Synthetic Aperture Radar: Wave Theory Foundations, Analysis and Algorithms*. Powder Springs, GA, USA: Barnes, 2015.
- [2] K. S. Chen, *Principles of Synthetic Aperture Radar Imaging*. Boca Raton, FL, USA: Taylor & Francis group, 2016.
- [3] B. Tso and P. Mather, *Classification Methods for Remotely Sensed Data*. Boca Raton, FL, USA: Taylor & Francis group, 2009.
- [4] I. Heidarpour Shahrezaei and H.-C. Kim, "Resolutional analysis of multiplicative high-frequency speckle noise based on SAR spatial de-speckling filter implementation and selection," *Remote Sens.*, vol. 11, no. 9, p. 1041, May 2019.
- [5] Q. Yan and W. Huang, "Sea ice remote sensing using GNSS-R: A review," *Remote Sens.*, vol. 11, no. 21, p. 2565, Nov. 2019.
- [6] D. A. Clausi and B. Yue, "Comparing cooccurrence probabilities and Markov random fields for texture analysis of SAR sea ice imagery," *IEEE Trans. Geosci. Remote Sens.*, vol. 42, no. 1, pp. 215–228, Jan. 2004.
- [7] F. Gao, X. Wang, Y. Gao, J. Dong, and S. Wang, "Sea ice change detection in SAR images based on convolutional-wavelet neural networks," *IEEE Geosci. Remote Sens. Lett.*, vol. 16, no. 8, pp. 1240–1244, Aug. 2019.
- [8] P. Ren, Z.-Q. Yu, G.-S. Dong, G.-X. Wang, and K. Wei, "Sea ice classification with first-order logic refined sliding bagging," *J. Coastal Res.*, vol. 90, no. sp1, pp. 129–134, Sep. 2019.
- [9] N. Y. Zakhvatkina, V. Y. Alexandrov, O. M. Johannessen, S. Sandven, and I. Y. Frolov, "Classification of sea ice types in Envisat synthetic aperture radar images," *IEEE Trans. Geosci. Remote Sens.*, vol. 51, no. 5, pp. 2587–2600, May 2013.
- [10] S. Leigh, Z. Wang, and D. A. Clausi, "Automated Ice–water classification using dual polarization SAR satellite imagery," *IEEE Trans. Geosci. Remote Sens.*, vol. 52, no. 9, pp. 5529–5539, Sep. 2014.
- [11] S. Das Peddada and J. T. G. Hwang, "Classification of pixels in a noisy grayscale image of polar ice," *IEEE Trans. Geosci. Remote Sens.*, vol. 40, no. 8, pp. 1879–1884, Aug. 2002.
- [12] A. Marino, W. Dierking, and C. Wesche, "A depolarization ratio anomaly detector to identify icebergs in sea ice using dual-polarization SAR images," *IEEE Trans. Geosci. Remote Sens.*, vol. 54, no. 9, pp. 5602–5615, Sep. 2016.
- [13] T. G. Yitayew, W. Dierking, D. V. Divine, T. Eltoft, L. Ferro-Famil, A. Rosel, and J. Negrel, "Validation of sea-ice topographic heights derived from TanDEM-X interferometric SAR data with results from laser profiler and photogrammetry," *IEEE Trans. Geosci. Remote Sens.*, vol. 56, no. 11, pp. 6504–6520, Nov. 2018.
- [14] L.-K. Soh and C. Tsatsoulis, "Texture analysis of SAR sea ice imagery using gray level co-occurrence matrices," *IEEE Trans. Geosci. Remote Sens.*, vol. 37, no. 2, pp. 780–795, Mar. 1999.
- [15] M. E. Shokr, "On sea-ice texture characterization from SAR images," *IEEE Trans. Geosci. Remote Sens.*, vol. 28, no. 4, pp. 737–740, Jul. 1990.
- [16] J. A. Nystuen and F. W. Garcia, "Sea ice classification using SAR backscatter statistics," *IEEE Trans. Geosci. Remote Sens.*, vol. 30, no. 3, pp. 502–509, May 1992.
- [17] B. R. Kerman, "Information states in radar imagery of sea ice," *IEEE Trans. Geosci. Remote Sens.*, vol. 37, no. 3, pp. 1435–1446, May 1999.

- [18] P. Maillard, D. A. Clausi, and H. Deng, "Operational map-guided classification of SAR sea ice imagery," *IEEE Trans. Geosci. Remote Sens.*, vol. 43, no. 12, pp. 2940–2951, Dec. 2005.
- [19] A. V. Bogdanov, S. Sandven, O. M. Johannessen, V. Y. Alexandrov, and L. P. Bobylev, "Multisensor approach to automated classification of sea ice image data," *IEEE Trans. Geosci. Remote Sens.*, vol. 43, no. 7, pp. 1648–1664, Jul. 2005.
- [20] H. Deng and D. A. Clausi, "Unsupervised segmentation of synthetic aperture radar sea ice imagery using a novel Markov random field model," *IEEE Trans. Geosci. Remote Sens.*, vol. 43, no. 3, pp. 528–538, Mar. 2005.
- [21] F. Berizzi, G. Bertini, M. Martorella, and M. Bertacca, "Two-dimensional variation algorithm for fractal analysis of sea SAR images," *IEEE Trans. Geosci. Remote Sens.*, vol. 44, no. 9, pp. 2361–2373, Sep. 2006.
- [22] H. Liu, L. Wang, and K. C. Jezek, "Automated delineation of dry and melt snow zones in antarctica using active and passive microwave observations from space," *IEEE Trans. Geosci. Remote Sens.*, vol. 44, no. 8, pp. 2152–2163, Aug. 2006.
- [23] S. Ochilov and D. A. Clausi, "Operational SAR sea-ice image classification," *IEEE Trans. Geosci. Remote Sens.*, vol. 50, no. 11, pp. 4397–4408, Nov. 2012.
- [24] G. Akbarizadeh, "A new statistical-based kurtosis wavelet energy feature for texture recognition of SAR images," *IEEE Trans. Geosci. Remote Sens.*, vol. 50, no. 11, pp. 4358–4368, Nov. 2012.
- [25] G. Zheng, X. Li, L. Zhou, J. Yang, L. Ren, P. Chen, H. Zhang, and X. Lou, "Development of a gray-level co-occurrence matrix-based texture orientation estimation method and its application in sea surface wind direction retrieval from SAR imagery," *IEEE Trans. Geosci. Remote Sens.*, vol. 56, no. 9, pp. 5244–5260, Sep. 2018.
- [26] U. Kandaswamy, D. A. Adjeroh, and M. C. Lee, "Efficient texture analysis of SAR imagery," *IEEE Trans. Geosci. Remote Sens.*, vol. 43, no. 9, pp. 2075–2083, Sep. 2005.
- [27] Z. Zeng and I. G. Cumming, "SAR image data compression using a tree-structured wavelet transform," *IEEE Trans. Geosci. Remote Sens.*, vol. 39, no. 3, pp. 546–552, Mar. 2001.
- [28] S. E. Grigorescu, N. Petkov, and P. Kruizinga, "Comparison of texture features based on Gabor filters," *IEEE Trans. Image Process.*, vol. 11, no. 10, pp. 1160–1167, Oct. 2002.
- [29] D. A. Clausi and H. Deng, "Design-based texture feature fusion using Gabor filters and co-occurrence probabilities," *IEEE Trans. Image Process.*, vol. 14, no. 7, pp. 925–936, Jul. 2005.
- [30] S. Solbo and T. Eltoft, "A stationary wavelet-domain Wiener filter for correlated speckle," *IEEE Trans. Geosci. Remote Sens.*, vol. 46, no. 4, pp. 1219–1230, Apr. 2008.
- [31] Y. Bian and B. Mercer, "Interferometric SAR phase filtering in the wavelet domain using simultaneous detection and estimation," *IEEE Trans. Geosci. Remote Sens.*, vol. 49, no. 4, pp. 1396–1416, Apr. 2011.
- [32] J. Singh and M. Datcu, "SAR image categorization with log cumulants of the fractional Fourier transform coefficients," *IEEE Trans. Geosci. Remote Sens.*, vol. 51, no. 12, pp. 5273–5282, Dec. 2013.
- [33] A. M. Atto, E. Trounev, J.-M. Nicolas, and T. T. Le, "Wavelet operators and multiplicative observation models—application to SAR image time-series analysis," *IEEE Trans. Geosci. Remote Sens.*, vol. 54, no. 11, pp. 6606–6624, Nov. 2016.
- [34] H. Q. Fu, J. J. Zhu, C. C. Wang, R. Zhao, and Q. H. Xie, "Atmospheric effect correction for InSAR with wavelet decomposition-based correlation analysis between multipolarization interferograms," *IEEE Trans. Geosci. Remote Sens.*, vol. 56, no. 10, pp. 5614–5625, Oct. 2018.
- [35] H. Q. Fu, J. J. Zhu, C. C. Wang, H. Q. Wang, and R. Zhao, "A wavelet decomposition and polynomial fitting-based method for the estimation of time-varying residual motion error in airborne interferometric SAR," *IEEE Trans. Geosci. Remote Sens.*, vol. 56, no. 1, pp. 49–59, Jan. 2018.
- [36] A. Mian, J.-P. Ovarlez, A. M. Atto, and G. Ginolhac, "Design of new wavelet packets adapted to high-resolution SAR images with an application to target detection," *IEEE Trans. Geosci. Remote Sens.*, vol. 57, no. 6, pp. 3919–3932, Jun. 2019.
- [37] H. Han, S.-H. Hong, H.-C. Kim, T.-B. Chae, and H.-J. Choi, "A study of the feasibility of using KOMPSAT-5 SAR data to map sea ice in the chukchi sea in late summer," *Remote Sens. Lett.*, vol. 8, no. 5, pp. 468–477, Jan. 2017.
- [38] I. Heidarpour Shahrezaei, M. Kazerooni, and M. Fallah, "A complex target terrain SAR raw data generation and evaluation based on inversed equalized hybrid-domain algorithm processing," *Waves Random Complex Media*, vol. 27, no. 1, pp. 47–66, Jun. 2016.
- [39] X. Chen, W. Huang, C. Zhao, and Y. Tian, "Rain detection from X-Band marine radar images: A support vector machine-based approach," *IEEE Trans. Geosci. Remote Sens.*, to be published.
- [40] A. K. Fung, *Microwave Scattering and Emission Models and Their Applications*. Norwood, MA, USA: Artech House, 2009.
- [41] J. Sun, X. Wang, X. Yuan, Q. Zhang, C. Guan, and A. Babanin, "The dependence of sea SAR image distribution parameters on surface wave characteristics," *Remote Sens.*, vol. 10, no. 11, p. 1843, Nov. 2018.
- [42] H. H. Arsenault and G. V. April, "Information content of images degraded by speckle noise," *Opt. Eng.*, vol. 25, no. 5, May 1986, Art. no. 255662.
- [43] S. A. Mallat, *A Wavelet Tour of Signal Processing, the Sparse Way*. Burlington, MA, USA: Academic, 2008.



IMAN HEIDARPOUR SHAHREZAEI was born in Isfahan, Iran, in 1985. He received the B.S. and M.S. (microwave engineering) degrees in telecommunication engineering from the University of Urmia, Urmia, Iran, in 2007 and 2011, respectively, and the Ph.D. degree in telecommunication engineering (microwave engineering) from the Malek Ashtar University of Technology (MUT), Tehran, Iran, in 2017.

Since 2018, he has been a Postdoctoral Research Analyst with the Korea Polar Research Institute and the Department of Remote Sensing. This department consists of a satellite remote sensing group and signal modeling sections. His current research interests include radar remote sensing, microwave imaging, synthetic aperture radars, raw data generation and evaluation, SAR image formation algorithm designing, and coherent image post-processing.



HYUN-CHEOL KIM (Member, IEEE) received the Ph.D. degree in earth and environmental sciences from Seoul National University, Seoul, South Korea, in 2006. His major is satellite oceanography. Since 2007, he has been working with the Korea Polar Research Institute (KOPRI) using satellite remote sensing data of the Arctic and Antarctic. From 2015 to 2016, he was the Head of the Remote Sensing Department, KOPRI. Since 2016, he has been the Director of the Unit

of Arctic Sea-Ice Prediction. This unit consists of a satellite remote sensing group and numerical modeling group, which mainly study the cryosphere and its climatic change. Notably, he is the first scientist to use KOMPSAT for polar science. He is actively involved in many international programs. He is a Korean Delegate of the IASC Cryosphere Working Group. He was a recipient of a Korea Prime Ministerial Citation for Excellence in Ocean Science, in 2019. He leads the Korean Polar Remote Sensing Group.

• • •